



Microstructural, morphological characterization and corrosion behavior of sand cast AlSi10Cu(Fe) alloy in chloride solution

Belkacem Korichi¹ · Nacer Zazi¹ · Stéphanie Delbrel² · Kieu Ngo² · Jean Paul Chopart³

Received: 17 October 2021 / Accepted: 3 January 2022 / Published online: 25 January 2022
© Institute of Chemistry, Slovak Academy of Sciences 2022

Abstract

In order to examine the relationship between the microstructure and the corrosion behavior in chloride solution, the microstructure of AlSi10Cu (Fe) sand cast aluminum alloy has been investigated by using different techniques including scanning electron microscopy, energy-dispersive spectroscopy, X-ray diffraction analysis and electrochemical measurements. The microscopic analysis and X-ray diffraction analysis show several phases in addition to matrix phase, including pores and phases at nano- and microscales. The average rate of micropores and nanopores is 4% and 5%, respectively. The nanoparticle size varies between 20 and 150 nm. Plates and corals-like silicon eutectic, rich-Cu phase and Chinese script phase ($\text{Al}_{15}(\text{Mn,Fe})_3\text{Si}_2$) have been observed. Energy-dispersive spectroscopy analyses show the presence of a new phase ($\text{Cu}_{61.22}\text{Zn}_{25.39}\text{Ni}_{11.85}\text{Al}_{1.54}$), and the pitting corrosion has been demonstrated to be initiated at the nanopores. The electrochemical measurements exhibited the effect of several elements and porosities on the corrosion kinetics that is controlled by charge transfer and diffusion phenomenon. Wide passive windows, followed by the breakdown of passive film and excessive dissolution, have been observed in 0.3 and 3 wt% NaCl solutions. The electrochemical measurements show a high corrosion rate which does not recommend the use of this alloy in seawater.

Keywords AlSi10Cu(Fe) cast alloy · Plates-like silicon eutectic · Corals-like silicon eutectic · $\text{Cu}_{61.22}\text{Zn}_{25.39}\text{Ni}_{11.85}\text{Al}_{1.54}$ phases · Aluminum corrosion · Nanopores

Introduction

Aluminum alloys are chosen as materials for construction in various fields due to their low density and their high corrosion resistance (Singh and Goel 1990). The aluminum–silicon alloys are economical and more lightweight due to the high quantity of silicon (Ahn et al. 2018). However, a high ratio of silicon in aluminum alloys can increase the cracking, the wear resistance and the fluidity of these alloys. Moreover, it can minimize the shrinkage porosity and reduce the

melting temperature point (Ahn et al. 2018; Elzanaty 2015). Therefore, the use of these alloys is limited due to the variations of their properties and their limited performance, especially at high temperature (Stadler et al. 2011, 2012; Ceschini et al. 2015).

The mechanical properties of these alloys depend on their microstructure, their chemical composition and their defects (Zamani et al. 2015; Campbell and Castings 2003; Jiang et al. 2014). In order to enhance their properties, some metallic elements including Mg, Cu, Fe, Ni and Sr have been added in addition to the silicon. In fact, the alloys microstructure is characterized by various present parts such as α -aluminum phase, primary silicon particles, aluminum–silicon eutectic, intermetallics and precipitates (Tenekedjiev and Gruzleski 1990; Bogdanoff et al. 2016).

The coral-like eutectic structure can be obtained by heat treatment or by addition of low concentrations of elements such as Na, Sr, or Eu which change the silicone plate-like eutectic morphology to fine and round coral-like eutectic morphology (Barrirero et al. 2019).

✉ Nacer Zazi
zazinacer@yahoo.fr; nacer.zazi@umtmo.dz

¹ Laboratoire de Mécanique, Structures et Energétique, Université Mouloud Mammeri de Tizi-Ouzou, 15000 Tizi-Ouzou, Algeria

² Sorbonne Université, Laboratoire Interfaces et Systèmes Electrochimiques, LISE, 75005 Paris, France

³ Université de Reims Champagne Ardenne, LISM EA 4695 UFR SEN, Moulin de la Housse, BP1039, 51687 Reims Cedex, France

The α -aluminum phase represents the matrix of cast aluminum–silicon alloys; it crystallizes in the appearance of non-faceted dendrites (Warmuzek 2004) and sometimes in appearance of non-dendritic forms (Zazi 2013). Moreover, the hard primary silicon particles distributed in the matrix are responsible for the good mechanical properties and the high wear resistance (Elzanaty 2015). (Oya et al. 2013) showed that the intergranular corrosion susceptibility increases as a function of the silicon content in the alloys.

Aluminum–silicon–magnesium alloys are polyphase materials and have good properties such as excellent castability, high ductility, high strength and low thermal expansion coefficient (Ahn et al. 2018; Cáceres et al. 2003). These properties explain why these alloys have occupied an important position in the field of automobile applications and are widely used in the production of engine components. The mechanical properties of these alloys depend on the size, the shape, the distribution, the degree of modification of eutectic phase, and the primary silicon particles (Ye 2003; Ma et al. 2017; Mohamed and Samuel 2012; Al-Hella and Kawther 2013). Moreover, the casting process plays a crucial role in the microstructure and mechanical properties of these alloys (Al-Hella and Kawther 2013).

In aluminum–silicon–magnesium cast alloys, the Mg-containing phases formed during the solidification are Mg_2Si , Si eutectic crystals and the π -Fe phase. The contents of Mg and Fe in these alloys and the solidification rate determine the fractions of the β -Fe and π -Fe phases and the concentration of Mg in solid solution. The π -Fe phase has a Chinese script or blocky morphology, and it is often formed on the β -Fe plates. The Mg_2Si phase ratio increases with the Mg content in the alloys, i.e., from close to zero for 0.3 wt% Mg to 0.2 vol% for 0.7 wt% Mg (Sjölander and Seifeddine 2010). The secondary phases, including Mg_2Si , π -Fe, β -Fe and Si eutectic crystals, can induce specific alloy properties and therefore have an influence on the mechanical and corrosion behavior of these materials (Dobkowska et al. 2016; Cecchel et al. 2017). In aqueous media, the corrosion resistance of aluminum and its alloys is provided by the formation of an oxide film composed of Al_2O_3 , $Al(OH)_3$ and $AlO(OH)$ phases on the metallic surface (Barr 1977). However, for media containing chloride ions, an extensive localized attack or a uniform corrosion can be observed (Bessone et al. 1992; Munoz and Bessone 1999; Allachi et al. 2010; Zazi et al. 2010). The oxide film on aluminum surface is a poor electronic conductor, and the cathodic reactions take place on the micron size intermetallic particles or smaller precipitate particles (Zaid et al. 2008). The silicon-rich phase can cause galvanic corrosion, and the porosities formed during the casting processes can generate crevice corrosion (Dobkowska et al. 2016)].

Several authors have showed the presence of Al_2Cu phase during the solidification of

aluminum–silicon–copper alloys (Sjölander and Seifeddine 2010; Dobkowska et al. 2016; Cecchel et al. 2017; Barr 1977; Bessone et al. 1992; Munoz and Bessone 1999; Allachi et al. 2010; Zazi et al. 2010; Zaid et al. 2008; Djurdjevic et al. 1999; Samuel et al. 1997; Li et al. 2003). This phase can be found in different shapes as compact block-like phase type, eutectic Al_2Cu phase type or mixture of both types. This Al_2Cu phase arises from β -Fe plate's phase or on coarse eutectic Si particles phase during the end of solidification process. Other phases including β - Mg_2Si , Θ - Al_2Cu , π - $Al_8Mg_3FeSi_6$, Q - $Al_5Cu_2Mg_8Si_6$, α - $Al_{15}(Fe,Mn)_3Si_2$ and β - Al_5FeSi can also be present in the alloys (Zazi et al. 2010; Li et al. 2003; Dinnis et al. 2006).

Porosities are cavities which are formed during the metal solidification. They are regarded to be the first defect that occurs in aluminum–silicon casting alloys (Ammar et al. 2008). These porosities can cause various issues such as poor mechanical properties with limited strength and ductility, variable fracture toughness and crack initiation sites (Ammar et al. 2008). The porosity development in solidifying aluminum–silicon casting alloys is due to shrinkage resulting from volume contraction associated with the solidification, and the entrapment of gas (mostly hydrogen and air) resulting from a decrease in gas solubility in the solid alloy compared to the liquid (Ammar et al. 2008). The formation of microporosities during the solidification of aluminum alloys is responsible for problems in the production of good quality products. Moreover, the process parameters during the solidification have a significant effect on the microstructural development of the alloy and determine the final engineering performance of the casting. Other parameters such as dendrite segregation, nature, size, distribution and morphology of precipitates and porosities have also a significant influence on mechanical and chemical alloys properties (Ferreira et al. 2010; Kuchariková et al. 2020).

The present work is a part of a larger research project (corrosion of AlSi cast alloys), which was performed to examine and to offer a better understanding of the influence of porosities (nano and micro size) and intermetallics on the corrosion behavior of AlSi10Cu(Fe) sand cast alloy containing zinc and to find the relationship between the microstructures and the corrosion behavior. The study has been achieved by investigation of microstructure of AlSi10Cu(Fe) sand cast aluminum alloy before and after two weeks of immersion in chloride solution (0.3 and 3 wt% NaCl) at room temperature and correlation with the observed corrosion phenomenon.

The microstructure was investigated by using optical microscopy, scanning electron microscopy (SEM), energy-dispersive spectroscopy (EDS), X-ray diffraction (XRD) and electrochemical measurements.

Experimental

Materials

The investigation materials were a hypoeutectic aluminum sand casting alloy AlSi10Cu(Fe), and the experimental samples were prepared from an industrial ingot from SNVI company (Aluminum Foundry Unit, Rouiba), Algeria.

The chemical composition of the alloy is shown in Table 1. The casting was carried out by gravitation in sand mold at temperatures between 700 and 750 °C.

The samples were cut into cubic form from the ingot by using a mechanical saw.

Alloy elaboration

The elaboration has been carried out by the use of melting and maintenance furnaces, and casting pockets with capacities of 350 kg, 150 kg and 50 kg, respectively.

A mixture of 160 kg of AlSi10Mg ingots with dimension of (720 × 100 × 80) mm³ delivered by PECHINEY added to 190 kg of returns (Runners, channels of casting, defective and rejected parts... etc.) was melted at a temperature between 700 and 750 °C, then cleaning and creaming were carried out, afterward the liquid mass was subjected to a degassing treatment, and finally the liquid metal was cast in the maintenance furnace at 750 °C, where the refining operation and a second cleaning were performed. 15 kg of the liquid metal has been cast in a casting pocket and then in sand molds. The obtained ingot was in dimensions of 300 × 100 × 60 mm³. No chemical composition correction, in the liquid mass, has been done during sand cast alloy elaboration.

Sample preparation and microstructure characterization

Metallographic observations were performed using optical microscopy. The samples were prepared by means of the standard metallographic procedure as follows: The samples were polished with emery paper from 600 to 4000 grit and then degreased with ethanol (from SIGMA ALDRICH Company, with purity ≥ 99.8%), cleaned with distilled water and finally dried in air. The etching process was performed in the solution composed of 99.9 in wt% H₂O (Monodistilled) and 0.1 in wt% NaOH (from SIGMA ALDRICH company, and purity ≥ 98.8%).

The sample surfaces were observed by optical microscopy and scanning electron microscopy before and after immersion during two weeks in aerated chloride solution of 0.3 wt% Microstructural analyses of the samples were carried out using a metallurgical microscopy (Carl Zeiss ICM405 microscopy) and a scanning electron microscopy (FEG Zeiss Ultra 55) equipped with an energy-dispersive spectrometer EDS (Bruker EDS Quantax).

The X-ray diffractograms of the materials were determined by XPERT PRO X-ray diffractometer at ambient temperature. The analyses of diffractograms (identification of aluminum peaks and intermetallic phases) were made by means of High Score software.

Electrochemical measurements techniques

The electrochemical measurements for 1.13-cm² samples immersed in sodium chloride solution 0.3 and 3 wt% NaCl at room temperature have been carried out. Using a potentiostat/galvanostat GAMRY Reference 600+ controlled by software GAMRY Framework. Input current /voltage range are 60 pA to 600 pA, – 24 to + 24 V, respectively.

A classic three-electrode method has been used. The reference electrode was a saturated calomel electrode (SCE); the auxiliary electrode was a platinum grid (3-cm²).

Potentiodynamic polarization tests have been undertaken with a scanning rate equal to 1 mV/s from – 1.2 to – 0.2 V according to the reference electrode.

The electrochemical impedance spectroscopy measurements was carried out in a frequency range from 100 kHz to 1 mHz and with a 10 mV potential modulation amplitude. To obtain accurate electrochemical impedance values, integration has been performed for seven cycles.

Results and discussion

The characterization of polished cast AlSi10Cu(Fe) aluminum alloy, both etched and non-etched samples, using optical microscopy is shown in Fig. 1. As it can be observed, the cast AlSi10Cu(Fe) aluminum alloy is characterized by a dendritic structure of the α -aluminum solid solution phase and two forms for the aluminum–silicon eutectic (silicon plate-like eutectic and coral-like eutectic). Firstly, unmodified silicon eutectic (silicon plate-like eutectic) is observed as it is for industrial solidifying conditions. Secondly, a modified coral-like eutectic phase is distributed over the entire sample surface with a low density as it is visible in Fig. 1e. Other secondary phases in

Table 1 Chemical composition of the elaborated AlSi10Cu (Fe) aluminum cast alloy

Element	Al	Si	Fe	Cu	Mn	Mg	Zn	Ni	Other
wt%	85.40	9.53	1.21	1.25	0.91	0.51	0.65	0.29	0.25

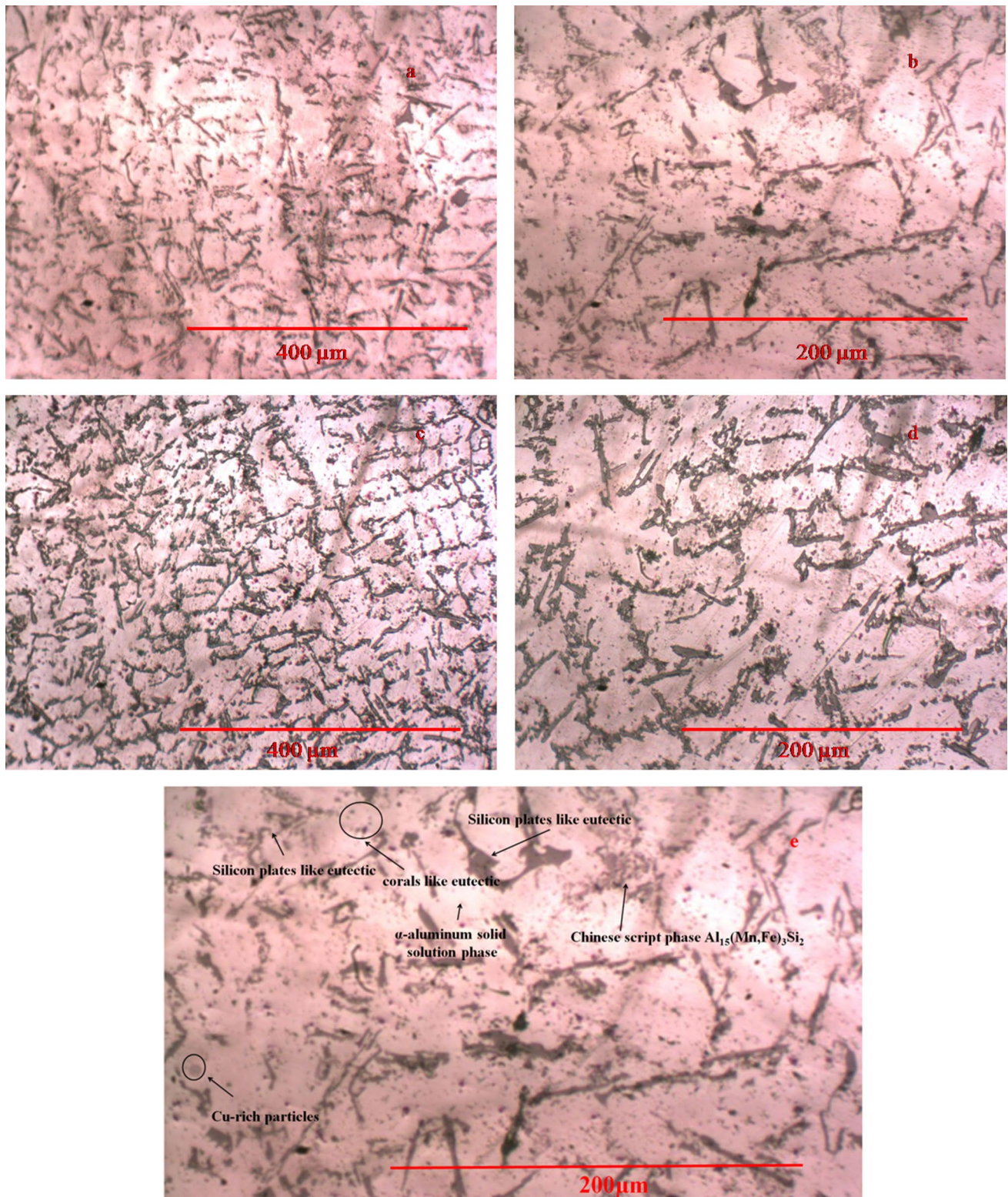


Fig. 1 Optical micrographs of AlSi10Cu(Fe) alloy: non-etched sample (a, b), etched sample (c, d), zoom of b (e)

the microstructure of the aluminum alloy such as rich-Cu phase and Chinese script phase $\text{Al}_{15}(\text{Mn,Fe})_3\text{Si}_2$ have been observed (Fig. 1). In order to identify the types of phases, EDS analysis has been used.

Micrographs of sand casting aluminum alloy AlSi10Cu(Fe) are shown in Fig. 2. For all figures, presence of pores and phases has been observed at micro- and nanoscales. The identified phases are α -Al matrix and Al-Si eutectic which appeared in the interdendritic space and intermetallic compounds.

The observed micro- and nanopores are due to hydrogen gas arising during melt casting because of a low speed cooling in sand casting: Hydrogen gas remains in the solidified melt in pores and micro-shrinkages, as described by (Michna et al. 2007). On the other hand, some pores are due to the effect of iron castability in AlSi10Cu(Fe) alloy; as reported by several authors (Taylor 1995; Mbuya et al. 2003; Roy et al. 1996), iron may degrade the castability of the alloys and an increase in iron content in alloy generates an increase in porosities rate. Moreover, the formation of iron-rich intermetallic phases can lead to the formation of shrinkage and porosity defects (Taylor 2004; Berlanga-Labari et al. 2020). An increase in iron content in alloys leads to an increase in hydrogen gas pressure in equilibrium, which is related to a given rate of dissolved gas. Moreover, the iron β - Al_5FeSi phase can provide pore nucleation sites (Mbuya et al. 2003; Roy et al. 1996). In our case, the mass percentage of iron in the alloy is equal to 1.21 wt% and the solubility of iron in the aluminum matrix is very low, i.e., 0.04 wt at 655 °C, and less than 0.01 wt% at room temperature. As a result, several iron-rich intermetallic particles can form during solidification, leading to the formation of porosities in the alloys. Other phases, Al_2Cu and sludge for example, restrict pore growth and expansion (Roy et al. 1996). It should be noted that the nanopores were only observed at the surface of the matrix.

As described in the literature (Tilloy et al. 2012), the size of micro- and nanoparticles and the morphology of intermetallic phases depend on various parameters such as chemical composition, solidification conditions and particularly heat treatment process. The used AlSi10Cu(Fe) cast aluminum alloy samples have not undergone heat treatments, leading to the presence of micro and nanoporosities with an average rate of 4% and 5%, respectively. The size of the observed nanoparticles varies between 20 and 150 nm.

SEM images associated with EDS spectra and chemical composition of a polished AlSi10Cu(Fe) cast aluminum alloy sample before immersion in chloride solution, for three zones, are shown in Figs. 3, 4, 5 and Tables 2, 3, 4, respectively. These figures show the matrix phase, the eutectic phase and different other secondary phases and particularly numerous chemical compositions for each secondary phase. These figures and the EDS spectra highlight that the samples are multicomponent aluminum alloys with various elements

(Al–Si–Cu–Fe–Mn–Mg–Zn–Ni). The details of chemical composition for each sample are shown in Tables 2, 3 and 4.

According to the literature, these elements have a low solubility at room temperature but in this case, their concentrations in the alloys are higher than their solubility in aluminum at ambient temperature (Mathers 2002; Reardon 2011; Ambat et al. 2006; McAlister and Murray 1987; Bannour et al. 2013; Skoko et al. 2009; Jia et al. 2018). It means that equilibrium is not reached; these elements may also exist in supersaturated solid solutions or in non-equilibrium intermetallic phases (Mathers 2002).

In Al-Si alloy, Al-Si multicomponent alloys or commercial and hypoeutectic alloys, several phases such as Al_2Cu , Mg_2Si , α - $\text{Al}_{12}(\text{Fe,Mn})_3\text{Si}_2$, β - Al_5FeSi , etc., have been reported by (Mbuya et al. 2003). In this work, a new phase $\text{Cu}_{61.22}\text{Zn}_{25.39}\text{Ni}_{11.85}\text{Al}_{1.54}$ has been evidenced, as it can be observed in Fig. 4 and Table 3.

The Fe containing insoluble phases can take place in different forms including large or small needles or platelets, Chinese script, spheroidal or globular, rosette-like, polygonal, hexagonal, polyhedral, star-like, clusters. Other shapes can also be observed, for examples π - $\text{Al}_8\text{Mg}_3\text{FeSi}_6$ in a Chinese script morphology, Al_5FeSi as needles, β - Al_5FeSi in platelet form, $\text{Al}_{15}(\text{Fe,Mn})_3\text{Si}_2$ in polyhedron forms, [$\text{Al}_{15}(\text{Fe,Mn,Cr})_3\text{Si}_2$] in sludge form (Mbuya et al. 2003; Roy et al. 1996; Taylor 2004; Tilloy et al. 2012). The large number of phases, the multicomponent aspect and the differences in the composition, form and phase size, for the aluminum–silicon alloys, do not facilitate the study of the corrosion behavior of these alloys.

Figure 6 shows the X-ray diffractogram of the aluminum AlSi10Cu(Fe) sand cast alloy. The aluminum peaks are observed in the diffractogram (Fig. 6a). All seventeen phases present in the alloy are shown in Fig. 6b and listed in Table 5. Three phases (7, 10 and 15) contain zinc, the phase (7) is close to the phase observed by EDS as described in Table 3 and Fig. 4, which confirms the presence of the $\text{Cu}_{61.22}\text{Zn}_{25.39}\text{Ni}_{11.85}\text{Al}_{1.54}$ phase.

Figures 7, 8, 9, 10 and 11 show the SEM images for several zones of AlSi10Cu(Fe) sand casting aluminum alloys, immersed in 0.3 wt% NaCl solution during two weeks. The corrosion morphology of the material after immersion in chloride solution is very complex. Independently of the contact between the second phases and the matrix, it seems that the generalized corrosion is extended over the matrix phase, as shown in Figs. 7d, e, 9a, b, 10c, d and 11a–c. The presence of second phases on the surface of the alloy promotes the formation of microgalvanic cells between the matrix and the second phases resulting in the corrosion of the matrix surrounding the second phases (Figs. 7d, e, 9a, b, 10a, b and 11b, c, e) or in the dissolution of second phases (Figs. 7a–c, 10c, d and 11b, c). The corrosion occurring on the matrix surrounding the

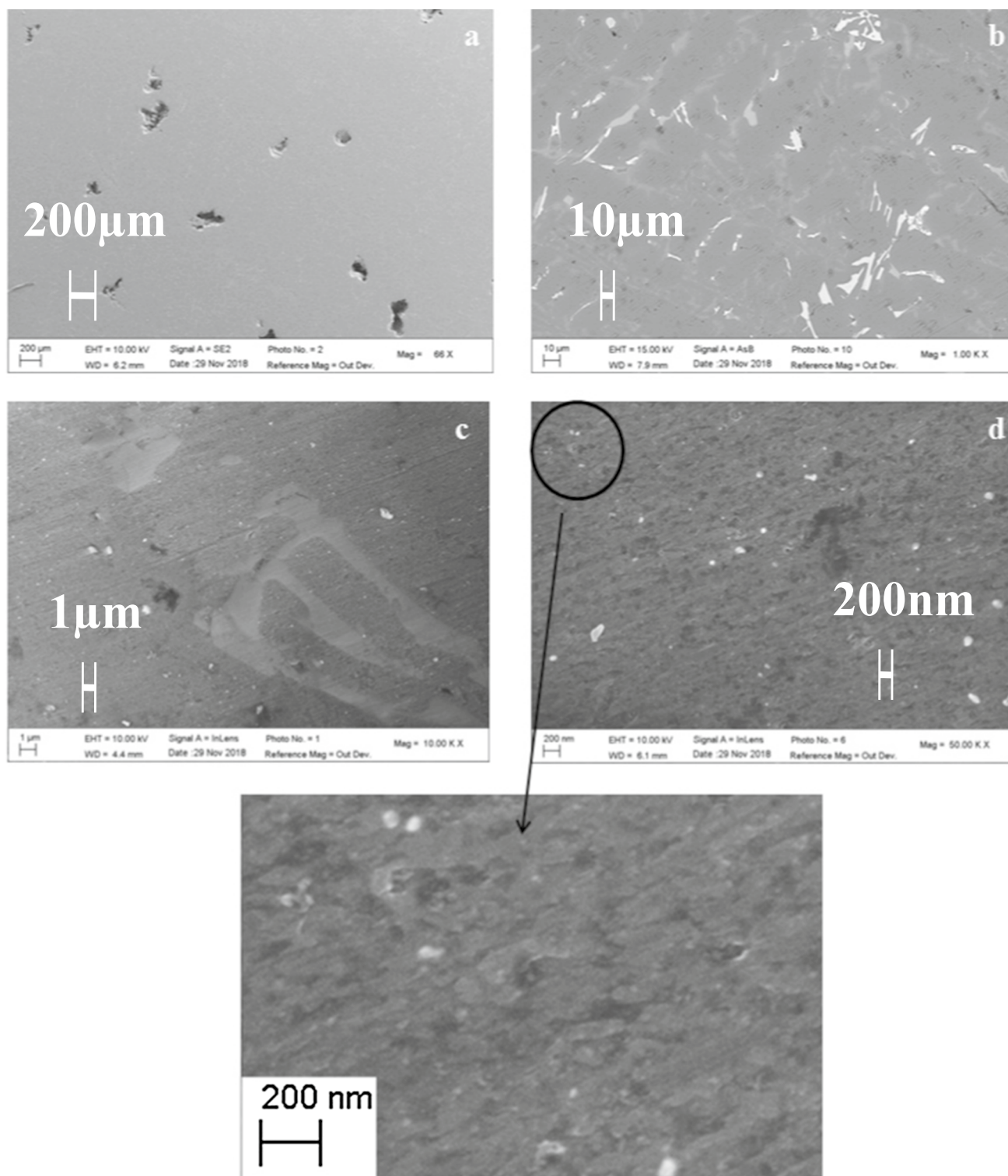


Fig. 2 SEM images of polished, non-etched samples of AlSi10Cu (Fe) cast aluminum alloy before immersion: (a, b) micropores, (c) microphases, and (d) nanophases and nanopores

second phases is due to the higher corrosion potential of the existing phases, as $\text{Al}_2\text{Cu}(\theta)$, AlFeMnSi , AlCuFeMn , AlCuFeSi and $(\text{Al,Cu})_x(\text{Fe,Mn})_y\text{Si}$, and the more active

aluminum matrix. According to the work of Birbilis and Buchheit (2005), the cathodic nature of these intermetallic phases compared to the matrix causes the reaction of

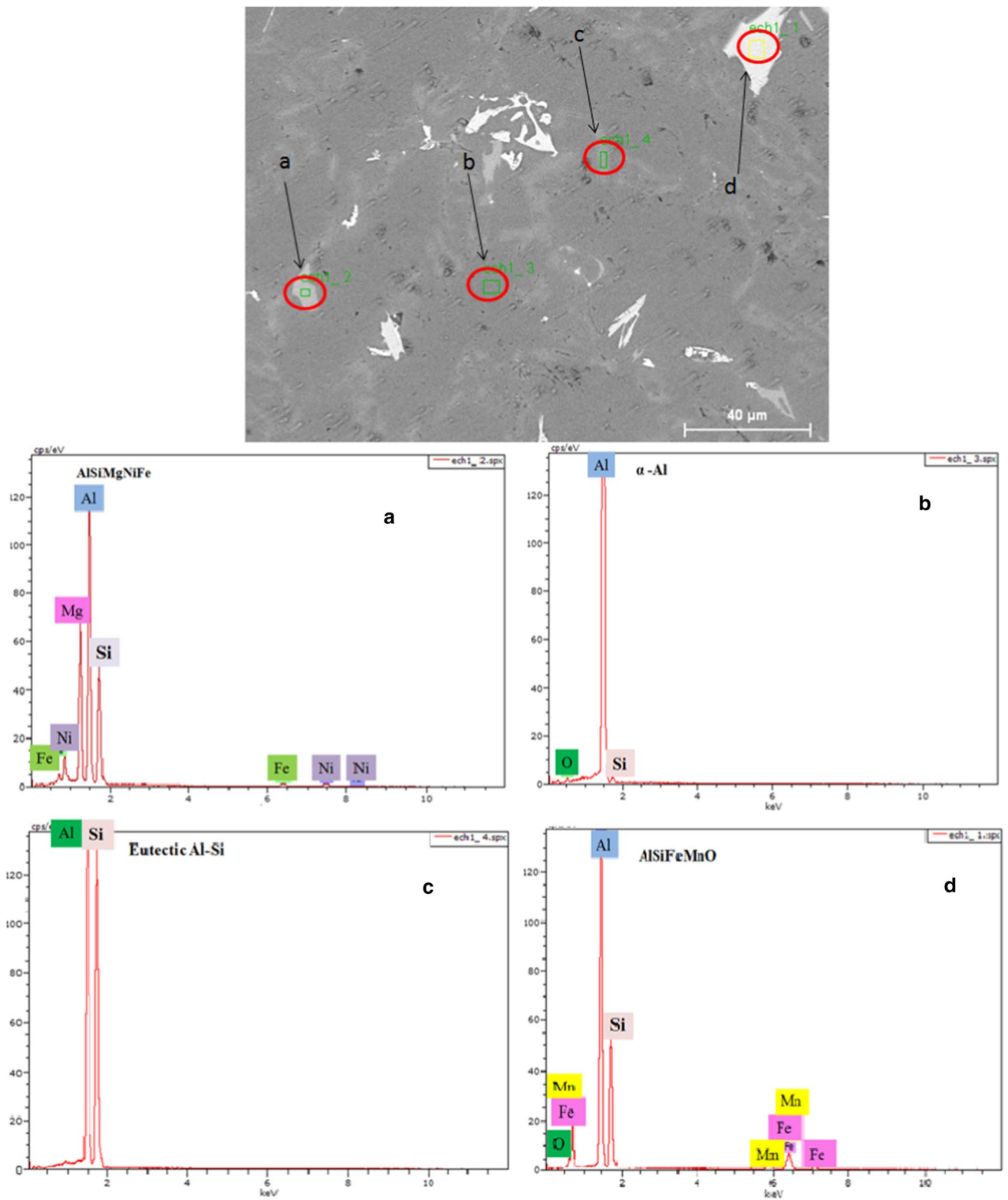


Fig. 3 SEM image and EDS spectra of points (a–d) in zone 1 for non-immersed sample

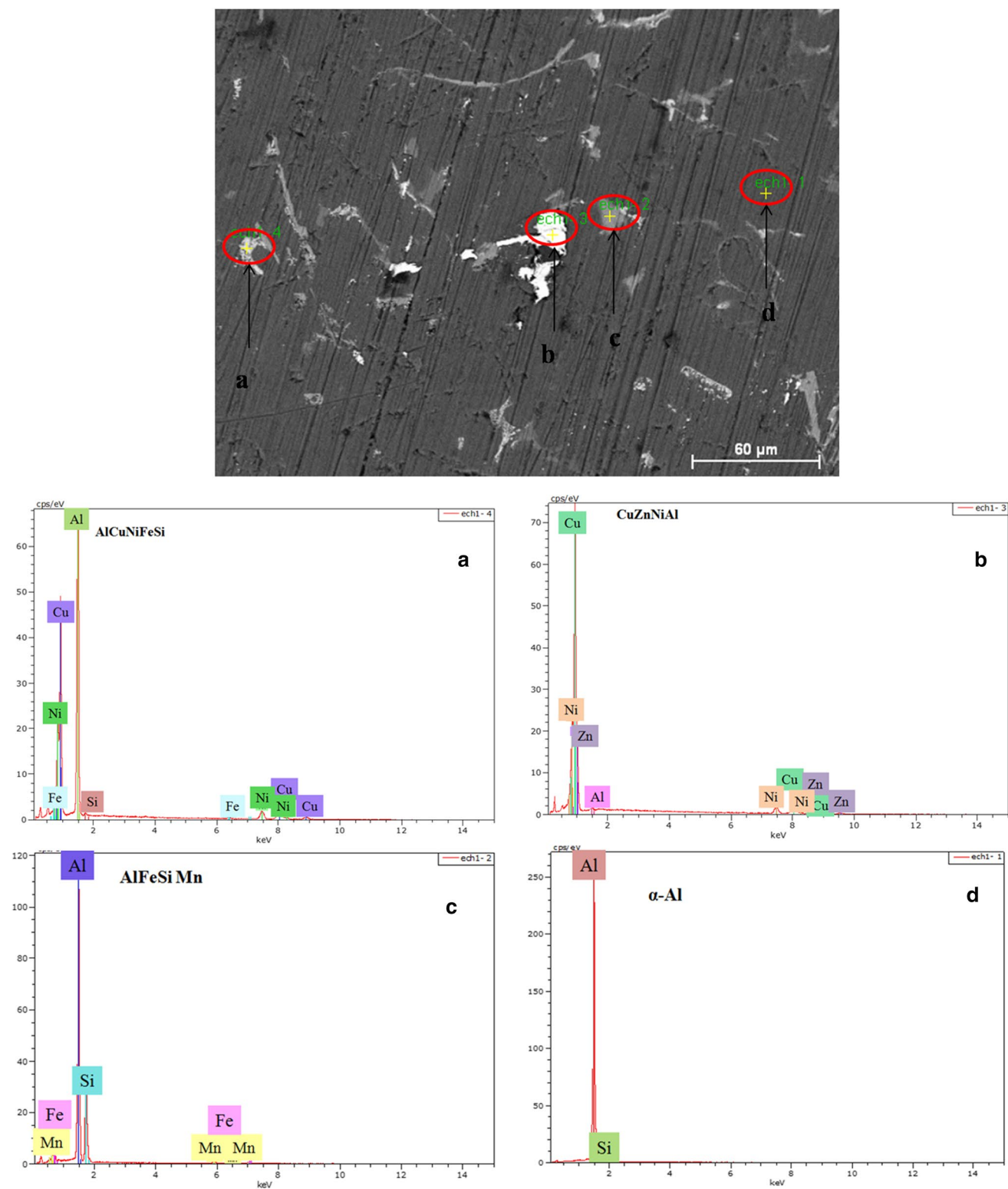


Fig. 4 SEM image and EDS spectra of points (a–d) in zone 2 for non-immersed sample

oxygen reduction on the intermetallic particles surface, leading to the formation of hydroxide ions. At the same time, a local increase in pH takes place, which provides

a breakdown of the flimsy oxide film and the dissolution of the area surrounding the intermetallic particles phases. The presence of iron, copper and nickel in intermetallic

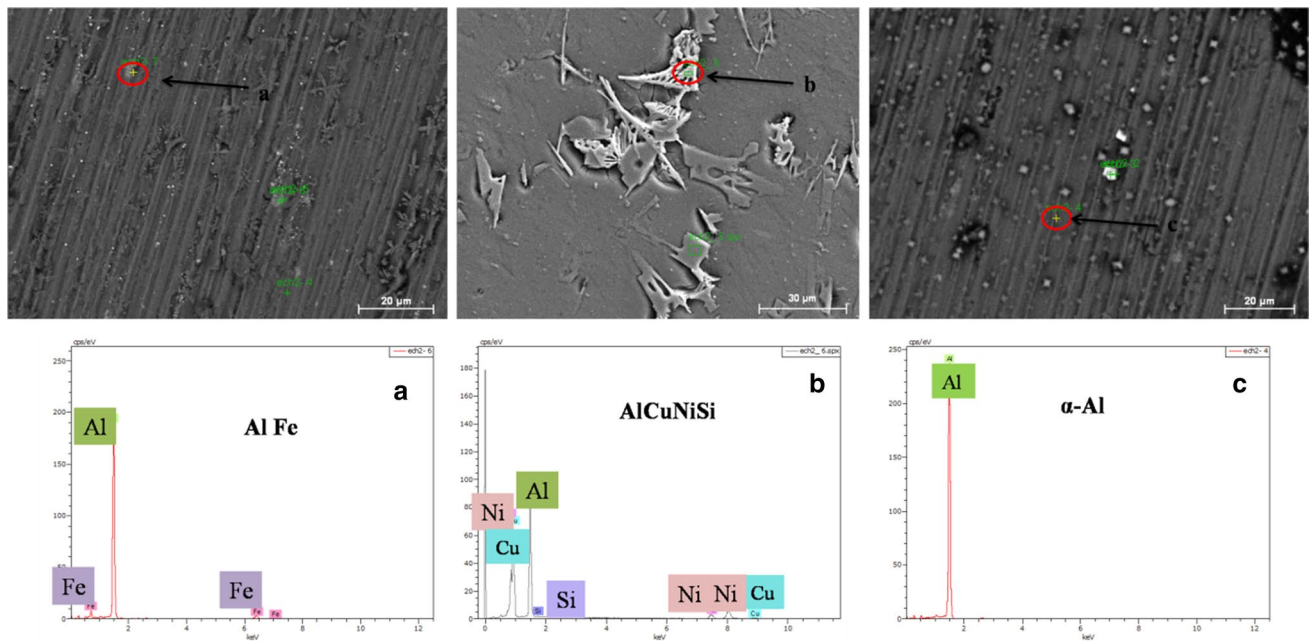


Fig. 5 SEM image and EDS spectra of non-immersed sample: **a** zone 3, **b** zone 4, **c** zone 5

Table 2 EDS results, chemical compositions, for some points of non-immersed sample in zone 1

Element	wt%	at. %	Element	wt%	at. %
<i>Point a, AlSiMgNiFe</i>			<i>Points b, α-Al</i>		
Mg _k	19.37	22.69	O _k	1.80	2.99
Al _k	42.05	42.05	Al _k	96.69	95.57
Si _k	26.77	26.77	Si _k	1.51	1.43
Fe _k	3.94	3.94			
Ni _k	7.87	7.87			
Total	100	100	Total	100	100
<i>Point c, Eutectic Al–Si</i>			<i>Point d, AlSiFeMnO</i>		
Al _k	46.47	47.47	Al _k	43.87	51.89
Si _k	53.53	52.53	Si _k	26.57	30.19
			Fe _k	25.84	14.77
			O _k	0.70	1.40
			Mn _k	3.02	1.76
			Total	100	100
Total	100	100	Total	100	100

Table 3 EDS results, chemical compositions, for some points of non-immersed sample in zone 2

Elements	wt%	at. %	Elements	wt%	at. %
<i>Point a, AlCuNiFeSi</i>			<i>Point b, CuZnNiAl</i>		
Al _k	35.40	55.73	Ni _k	11.06	11.85
Si _k	0.27	0.40	Cu _k	61.87	61.22
Ni _k	14.48	10.48	Zn _k	26.41	25.39
Cu _k	49.20	32.89	Al _k	0.66	1.54
Fe _k	0.65	0.49			
Total	100	100	Total	100	100
<i>Point c, AlSiFeMn</i>			<i>Point d, α-Al</i>		
Al _k	47.95	58.15	Al _k	98.09	98.16
Si _k	19.55	22.78	Si _k	01.91	01.84
Fe _k	29.28	17.16			
Mn _k	03.22	01.92			
Total	100	100	Total	100	100

phases has a determinant effect on the alloy resistance in chloride solution (Ambat et al. 2006; Seri et al. 1989; Hos-sain et al. 2015). The dissolution of intermetallic particle phases, and/or less noble segregated elements, is characterized by a perforation encircled by white circles, surrounding the β-Fe plate phases, as observed in Fig. 11f. In this case, the dissolved intermetallic particles are less noble than the surrounded phases and the matrix phases, and the same phenomenon occurs between the nobler

phases (matrix and surrounded phases) and the dissolved phase. According to Birbilis and Buchheit (2005), this can be due to the fact that the dissolved phases contain one, two or all elements which are contained in the alloy, including zinc, magnesium and manganese.

The dissolution of the α-aluminum phase in silicon eutectic is shown in Figs. 7a–c, 10b–d and 11a–c. This dissolution can be explained by the potential difference between α-aluminum phase and silicon phase since the silicon phase potential is always higher than the α-aluminum phase potential in chloride solution (Birbilis and Buchheit 2005).

Table 4 EDS results, chemical compositions, for some points of non-immersed sample in zone 3

Elements	wt%	at. %	Elements	wt. %	at. %
<i>Zone 3 (a) Al Fe</i>			<i>Zone 4(b) AlCuNiSi</i>		
Al _k	87.98	93.81	Al _k	38.38	58.73
Fe _k	12.02	0.49	Si _k	0.31	0.46
Total	100	100	Cu _k	44.12	28.68
			Ni	17.19	12.10
			Total	100	100
<i>Zone 5(c) α-Al</i>					
Al _k	100	100			
Total	100	100			

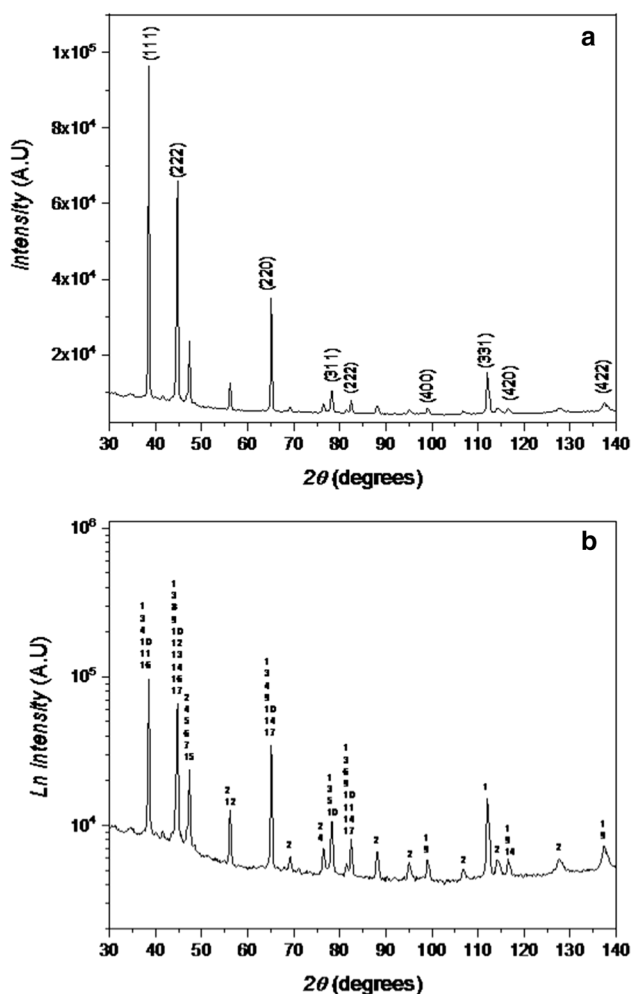
**Fig. 6** X-ray spectrum of the aluminum AlSi10Cu(Fe) sand cast alloy: **a** aluminum diffraction plans and **b** all seventeen phases in the alloy

Figure 9 shows the formation of several hemispherical pits in certain zones or only one pit in other zones. The authors observed also a localized corrosion with crater shape in the

nanopores of the matrix phases (Fig. 8). We assume that the pit beginning occurs at nanopore level.

Small white 50–200 nm size intermetallic particles can be observed in Figs. 7b–d, 10c, d and 11e, f. Particles of approximately 50 nm size were observed on the silicon plates-like eutectic (Fig. 7b, c) and coral-like eutectic phases (Fig. 7d). These particles were not dissolved after two weeks of immersion in chloride solution, meaning that their corrosion potential is higher than those of all other present phases.

SEM images associated with EDS spectrum and chemical composition of AlSi10Cu(Fe) cast aluminum alloy after two weeks of immersion in chloride solution are shown in Fig. 12 and Table 6, respectively. Two points (a and b) in zone 6 have been chosen in the areas adjacent to the pits.

We observe the presence of oxygen, magnesium, aluminum, chlorine, carbon and oxygen in point a, and aluminum, silicon, magnesium and chlorine in point b. This result is in accordance with (Yoo et al. 2011). Moreover, the formation of a homogeneous layer of hydrated aluminum oxide surrounding the pit has been identified, confirming a pitting corrosion mechanism. In fact, hydrated and dehydrated aluminum oxides can be formed when aluminum is exposed to a solution containing aggressive ions, as in our case (Pourbaix 1974). The EDS analyses showed also the presence of carbon traces.

Electrochemical analyses including current–potential curves and electrochemical impedance spectroscopy of AlSi10Cu(Fe) sand cast alloy immersed in 0.3 and 3 wt% NaCl solutions for different times are shown in Figs. 13, 14, 15, 16, 17, 18, 19, 20 and Tables 7, 8, 9, 10.

Figure 13 shows difference in corrosion kinetics between the first hour of immersion and after two weeks of immersion in a 0.3 wt% NaCl solution. A large decreasing of corrosion potential was observed, from -0.583 V after 1-hour immersion to about -1.09 V after two weeks. Moreover, a weak increase in polarization resistance is observed after two weeks, i.e., from 2.5 k Ω to 2.8 k Ω (Table 7). In Figs. 14 and 15, we observe a huge corrosion potential decrease from -0.583 to -1.140 V, between 1-h and 7-day immersion, followed by a corrosion potential increase up to -1.097 V after two weeks of immersion. A large increase in polarization resistance was observed between 1- and 24-h immersion, from 2.5 to 16.5 k Ω , thereafter a decrease until 7 days, from 16.5 to 2.1 k Ω , and finally an increase to 2.8 k Ω after 14 days (Table 7). The variations in corrosion potential and polarization resistance are due to an oxide layer formation and the dissolution of noble metals on the alloy surface.

The corrosion rate is determined using the following relation (Rossi et al. 2007):

$$v = \frac{A_{i, \text{corr}}}{n \cdot F \cdot \rho} \quad (1)$$

Table 5 Seventeen phases present in AlSi10Cu(Fe) sand cast alloy

Phase number	Chemical formula	Diffraction angle 2θ ($^\circ$)	Diffraction plans (hkl)
1	Al	38.47, 44.718, 65.094, 78.226, 82.431, 99.081, 112.046, 116.574, 137.463	(1 1 1), (2 0 0), (2 2 0), (3 1 1), (2 2 2), (4 0 0), (3 3 1), (4 0 0), (4 0 2)
2	Si	47.313, 56.135, 69.144, 76.395, 88.054, 94.976, 106.937, 114.124, 127.587, 136.946	(2 2 0), (3 1 1), (4 0 0), (3 3 1), (4 2 2), (5 1 1), (4 4 0), (5 3 1), (6 2 0), (5 3 3)
3	Al ₉ Si	38.498, 44.751, 65.144, 78.289, 82.701	(1 1 1), (0 0 2), (0 2 2), (1 1 3), (2 2 2)
4	Al ₈ FeMg ₃ Si ₃	38.695, 65.003, 76.322	(2 0 2), (4 0 0), (3 2 2)
5	Al ₉ Fe ₂ Si ₃	45.603, 78.780	(8 2 0), (3 5 0)
6	Al ₂ Cu	47.569, 82.352	(3 1 0), (3 2 3)
7	Ni ₇ Cu ₃ Zn ₁₀	47.359	(2 0 0)
8	Al ₉ Fe _{0.84} Mn _{2.16} Si	44.682	(2 0 3)
9	Fe ₇ Ni ₃	44.762, 65.161, 82.524, 99.198, 116.732, 137.713	(1 1 0), (2 0 0), (2 1 1), (2 2 0), (3 1 0), (2 2 2)
10	Al _{3.8} Zn _{0.2}	38.568, 44.833, 65.271, 78.451, 82.675	(1 1 1), (0 0 2), (0 2 2), (1 1 3), (2 2 2)
11	Al ₆ CuMg ₄	38.269, 82.352	(1 1 0), (0 2 2)
12	Cu _{3.17} Si	44.600	(1 0 0)
13	Al ₉ Mn ₃ Si	44.780	(0 2 3)
14	Mn ₃ Si	44.762, 65.161, 82.524, 116.732	(2 2 0), (4 0 0), (4 2 2), (6 2 0)
15	ZnNi	47.488	(0 2 2)
16	AlCu	38.853, 44.763	(3 0 0), (3 1 0)
17	Cu ₃ Si	44.537, 65.238, 82.267	(0 1 2), (0 0 3), (2 5 0)

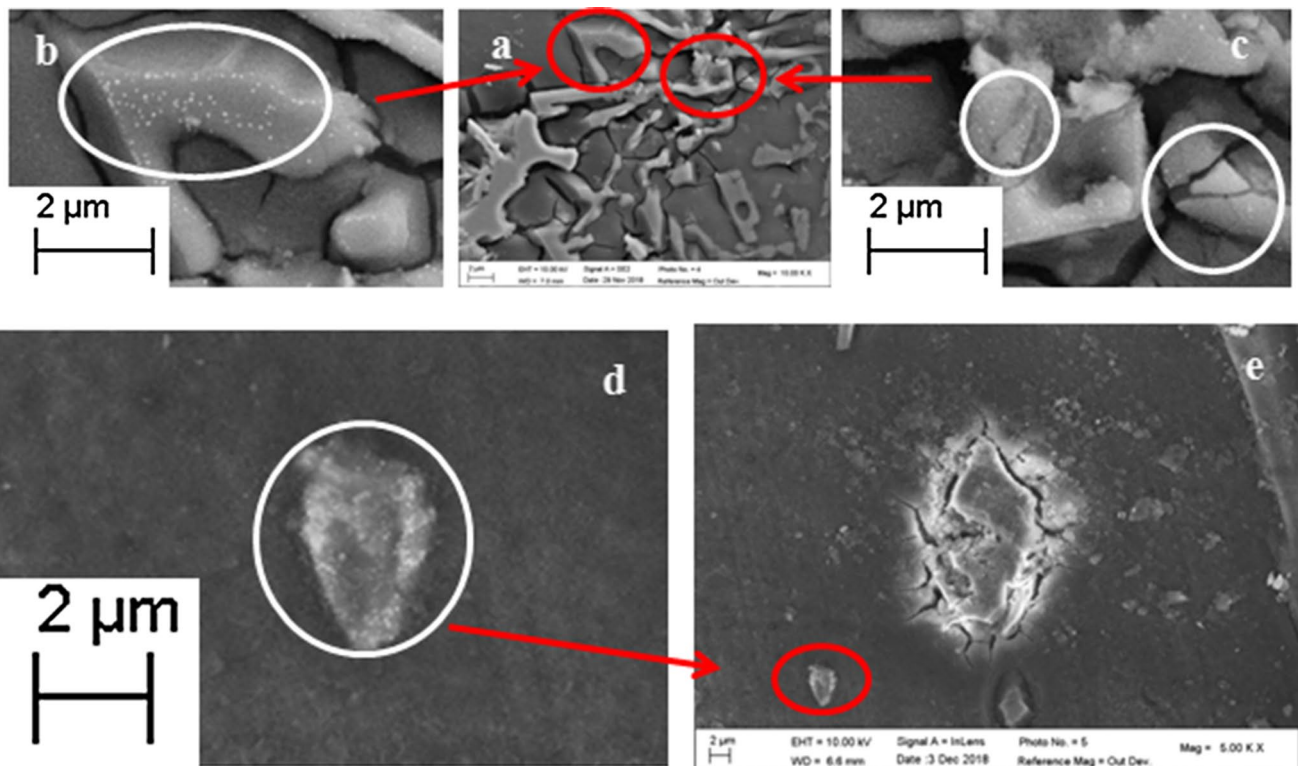


Fig. 7 SEM images of non-polished AlSi10Cu(Fe) sand cast aluminum alloy after two weeks of immersion in 0.3 wt% NaCl solution (**a, e**). Dissolution of α -aluminum phase surrounding second phases,

b, c magnification of SEM image presented in **a**, **d** magnification of SEM image presented in **e**, **b–d** small white intermetallic particles

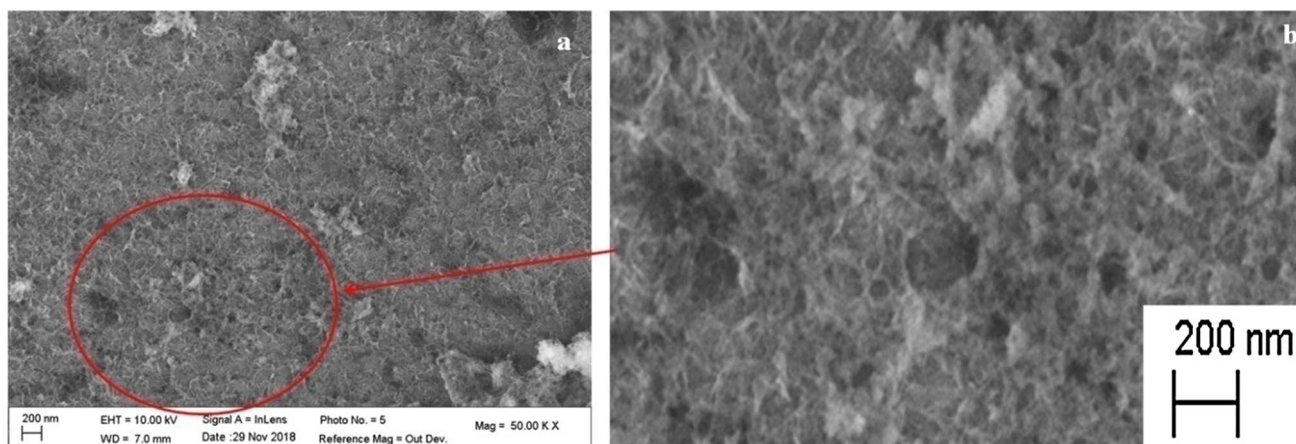


Fig. 8 SEM images of non-polished AlSi10Cu (Fe) sand cast aluminum alloy after 15 days of immersion in 0.3 wt% NaCl solution: **a** corrosion presence at the nanopores, **b** magnification of SEM image presented in **a**

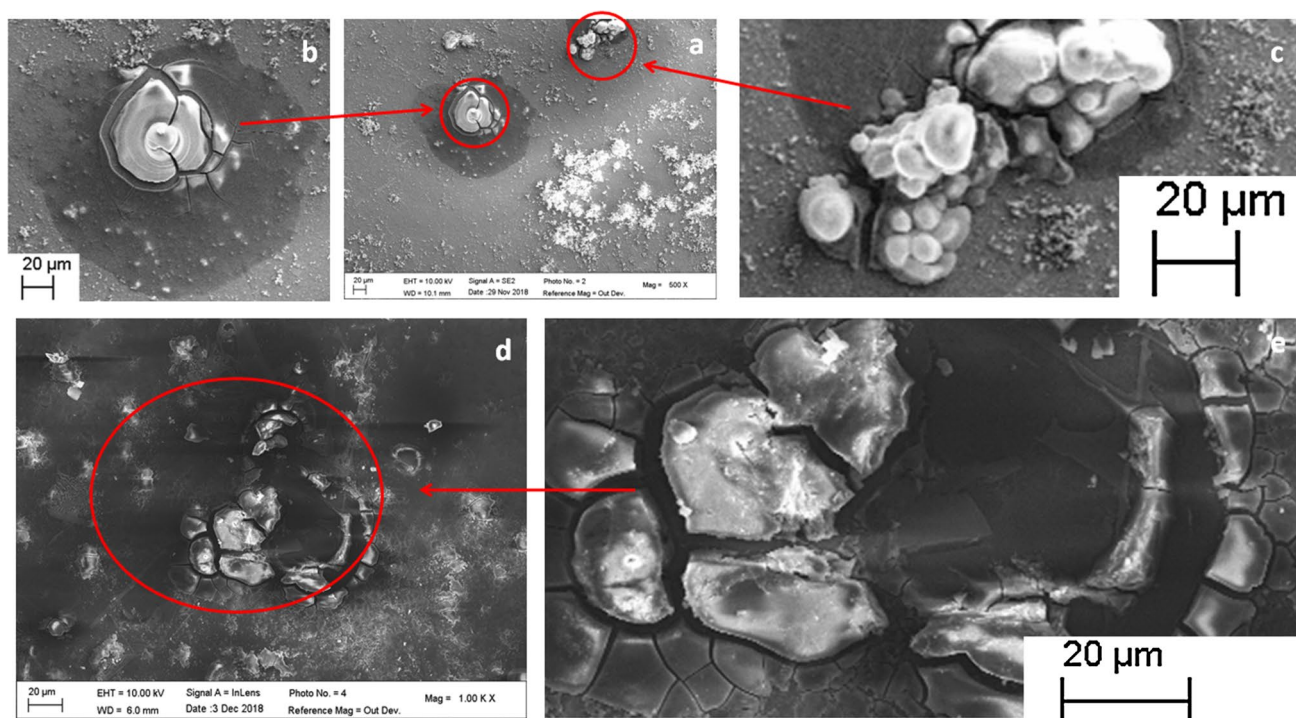


Fig. 9 SEM images of non-polished AlSi10Cu (Fe) sand cast aluminum alloy after two weeks of immersion in 0.3 wt% NaCl solution: **a, d** hemispherical pits, **b, c** magnification of SEM image presented in **a**, **e** magnification of SEM image presented in **d**

where A is material molar mass (g/mol.), i_{corr} current corrosion density ($\mu\text{A}/\text{cm}^2$), n exchanged electrons number, and F Faraday constant = 96500C, ρ Density of metal (g/cm^3).

The corrosion rate increases from 0.043 mm/year after 1 h of corrosion to 0.274 mm/year after 7-day immersion and decreases to 0.172 mm/year after 2 weeks.

Wide passive zones, followed by the breakdown of passive film and excessive dissolution, were observed after corrosion during three, seven days and two weeks, and their

values are ~ 570 mV, ~ 544 mV, ~ 500 mV, respectively (Fig. 14).

The corrosion behavior of the alloy is similar in 3 wt% NaCl solution. Figures 16, 17 and 18 show a difference in corrosion kinetics between the first hours until two weeks of immersion. A large corrosion potential decrease is observed, from -0.935 V after one hour and -1.105 V after one week, and then an increase to -1.092 V after two weeks. The polarization resistance decreases from 21 k Ω after 1 h

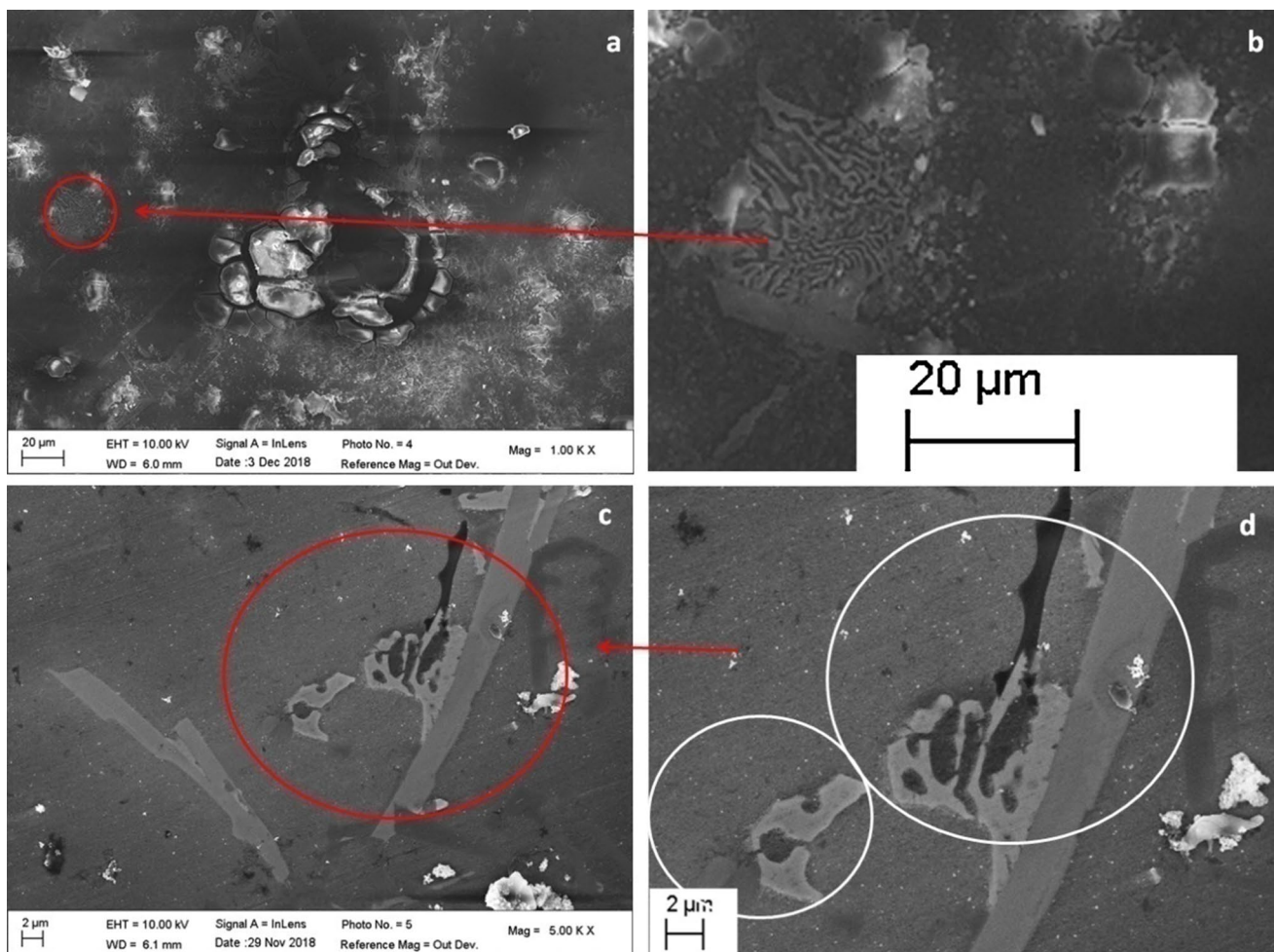


Fig. 10 SEM images of non-polished AlSi10Cu(Fe) sand cast aluminum alloy after two weeks of immersion in 0.3 wt% NaCl solution: **a, c** dissolution of α -aluminum phase surrounding eutectic phase, **b, d** magnification of SEM image presented in **a, c**

of immersion to 0.5 k Ω after 3 days of corrosion and then increases up to 1.4 k Ω after two weeks (Table 8). The corrosion rate increases from 0.017 mm/year after 1 h of immersion to 0.466 mm/year after one week. Due to this high value, the use of this alloy is not recommended for seawater.

The increase in NaCl concentration in the solution greatly modifies corrosion potential values and polarization resistances during the first hour of immersion. In both cases, the polarization resistance is the highest at the first hour and the corrosion potential converges to the same value after two weeks of immersion. The modification of the corrosion kinetics is probably due to pitting corrosion phenomenon (Figs. 9, 10), appearance and disappearance of microporosities and nanoporosities on the surface, presence of less noble elements segregated or not and particles dissolution as a function of the immersion duration.

Wide passive windows, followed by the breakdown of passive film and excessive dissolution, were observed after twenty four hours, three days, seven days and two weeks of corrosion with values equal to ~429 mV, ~465 mV, ~493 mV, ~470 mV, respectively (Fig. 18).

Figure 19 shows the Nyquist plots of impedance of the alloy immersed in 0.3 wt% NaCl solution. In all diagrams, a charge transfer loop at high frequency followed by a diffusion phenomenon at low frequency is observed; the result is in good agreement with (Frers et al. 1990, Jafarzadeh et al. 2009 and Fernandes et al. 1989). The charge transfer loop is directly related to electrochemical transfer reactions, typically due to the metallic dissolution occurring on the alloy surface, for example:



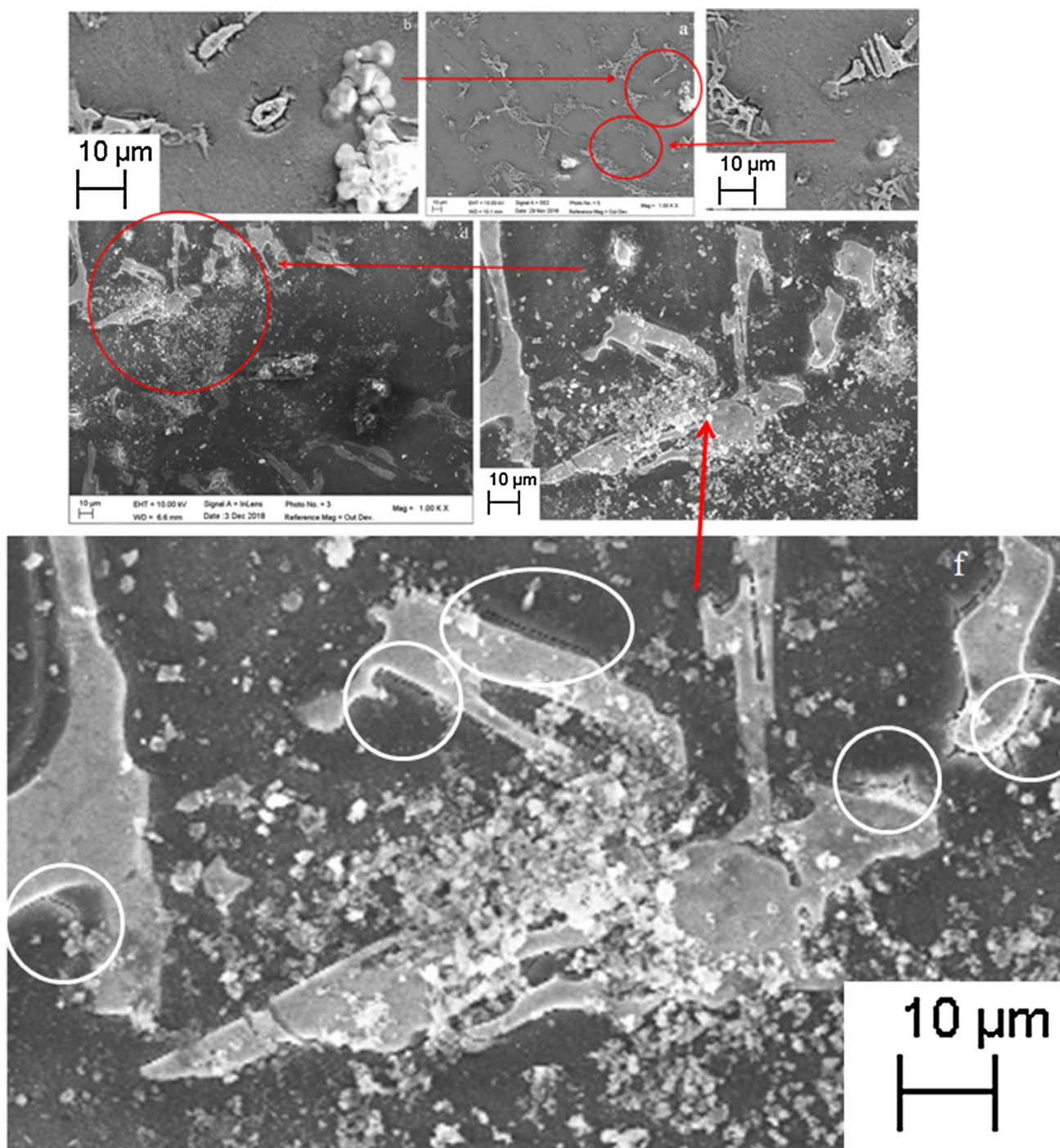
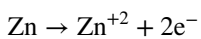


Fig. 11 SEM images of non-polished AlSi10Cu(Fe) sand cast aluminum alloy after two weeks of immersion in 0.3 wt% NaCl solution: **a, c, d** extended generalized corrosion, **b, c, e** corrosion on the matrix surrounding the second phases, **b, c, f** dissolution of second phases

and,



(3)

The transfer resistance value increases with immersion time, from 554 Ω after one hour to 2768 Ω after two weeks of immersion (Table 9).

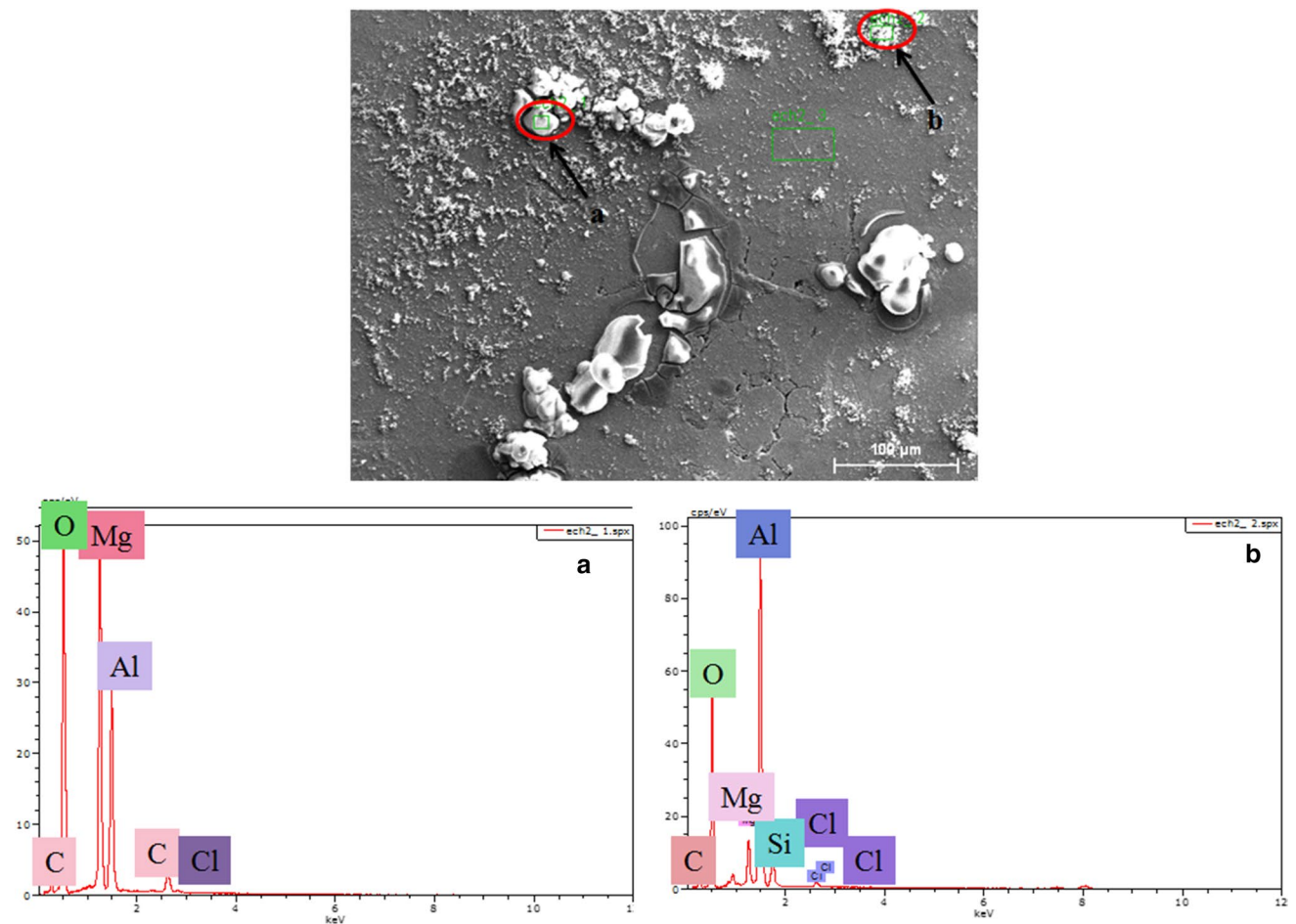


Fig. 12 SEM image and EDS spectra of points (a, b) in zone 6 of AlSi10Cu(Fe) sand cast aluminum alloy after two weeks of immersion in 0.3 wt% NaCl

Table 6 EDS results, chemical composition, in some region of two weeks of corroded sample in 0.3 wt% NaCl

Element	wt%	at. %	Element	wt%	at. %
<i>Point a</i>			<i>Point b</i>		
O _k	60.71	71.39	O _k	47.00	59.88
Mg _k	21.31	16.49	Mg _k	5.04	4.23
Al _k	15.46	10.78	Al _k	40.61	30.68
Cl _k	2.52	1.34	Cl _k	0.85	0.49
			Si _k	6.50	4.72
Total			Total	100	100

The diffusion (Warburg) line is representative of the transport phenomenon, toward the porous surface layer of the alloy.

An analysis of the high-frequency loop allows determining the double-layer capacitance and transfer resistance

values. The double-layer capacitance C_d values are not constant according to the immersion times (Table 9); this is probably due to an evolution of the passive layer thickness on the alloy surface, the localized corrosion process, and the presence of porosities. The increase of the transfer resistance value can be explained by the increase in the oxide layer thickness (Zazi et al. 2010).

The impedance spectra of AlSi10Cu(Fe) sand cast aluminum alloy immersed in 3 wt% NaCl solution are presented in Fig. 20, and the characteristics of the impedances curves are given in Table 10. As for the previous case, the diagrams show a charge transfer loop, followed by a diffusion phenomenon. The charge transfer resistance (R_t) increases with immersion time, from 271 Ω after one hour up to 2536 Ω after two weeks of immersion. However, the double layer capacitance (C_d) values decrease from 587 μF after one hour up to 323 μF after two weeks of immersion.

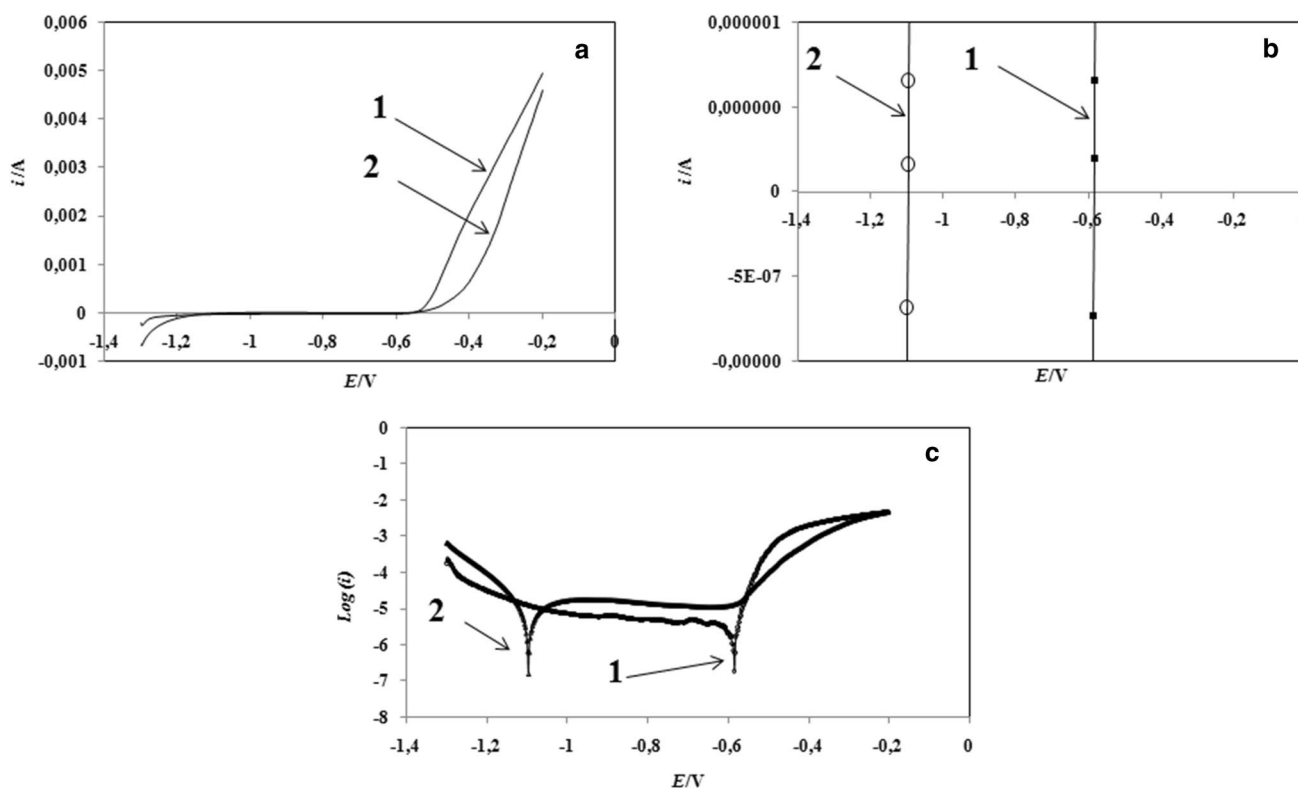
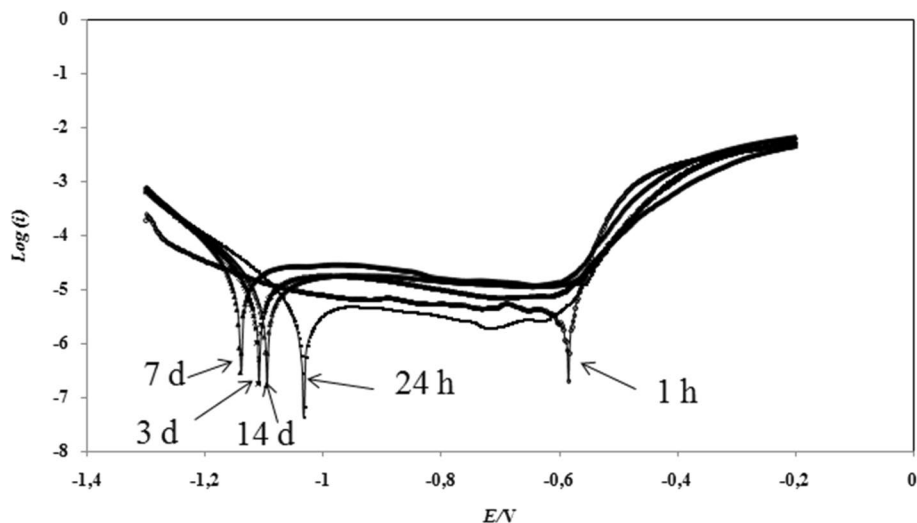


Fig. 13 Polarization curves of AlSi10Cu(Fe) sand cast aluminum alloy after 1 h immersion in 0.3 wt% NaCl solution (curve 1), and after 14 days of corrosion (curve 2) in 0.3 wt% NaCl solution: **a** $i(E)$ curves, **b** magnifying effect of $i(E)$ polarization curves, and **c** $\log i(E)$ curves

Fig. 14 $\text{Log}i(E)$ curves of AlSi10Cu(Fe) sand cast aluminum alloy after immersion in 0.3 wt% NaCl solution for duration of: 1 h, 24 h, 3 days, 7 days, and 14 days



Conclusions

The present work was performed to examine and to offer a better understanding of the influence of several intermetallics and porosities (nano and microporosities) on the corrosion behavior of AlSi10Cu(Fe) sand cast alloy containing zinc and to find the relationship between the microstructure

and the corrosion behavior. Microstructure characterization and corrosion behavior of aluminum AlSi10Cu(Fe) sand cast alloy in chloride solution were investigated. The main results can be summarized as.

The chemical composition of the different second phases present in the alloy is variable, several phases and a new phase $\text{Cu}_{61.22}\text{Zn}_{25.39}\text{Ni}_{11.85}\text{Al}_{1.54}$, white nanoparticles on a

Fig. 15 Magnification of $i(E)$ curves of AlSi10Cu(Fe) sand cast aluminum alloy after immersion in 0.3 wt% NaCl solution for duration of: 1 h, 24 h, 3 days, 7 days, and 14 days

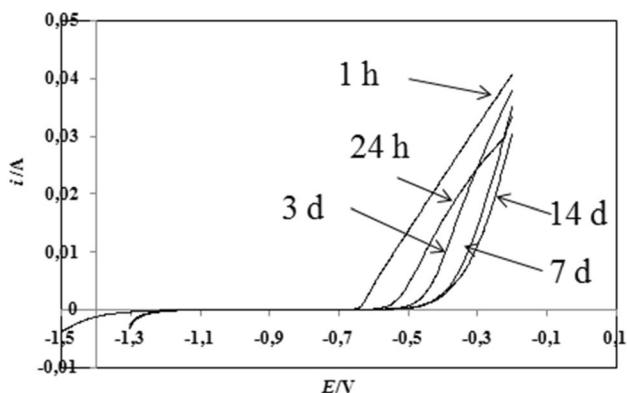
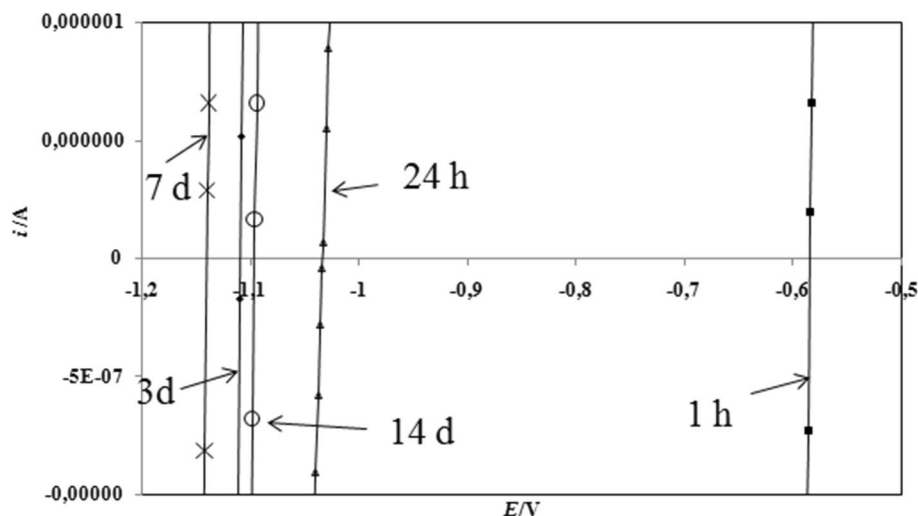


Fig. 16 $i(E)$ curves of AlSi10Cu(Fe) sand cast aluminum alloy in 3 wt% NaCl solution after different immersion times

silicon plate-like eutectic and coral-like eutectic have been observed.

Dissolution of aluminum phase surrounding the eutectic phases, and dissolution of fine particles and/or segregation

surrounding the β -Fe plates phases occur. Nanopores on the surface of the samples have been characterized and can be responsible for the pitting corrosion, and the analysis of pitting zones shows that the zones contain oxygen, aluminum, silicon, magnesium and chlorine.

The Nyquist plot evidences a charge resistance transfer at high frequency followed by a diffusion phenomenon (Warburg line) at low frequency. Impedance measurements show dissolution of metals on the alloy and electrolyte diffusion toward the porous surface layer of alloy, without adsorption phenomenon. It can be assumed that the corrosion phenomena are due to the appearance and the disappearance of porosities and the dissolution of less noble elements.

The transfer resistance is about 2.7 k Ω in 0.3 wt% NaCl and 2.5 k Ω in 3 wt% NaCl after two weeks of immersion, and the double-layer capacitance is about 200 μ F in the 0.3 wt% NaCl solution and 300 μ F in 3 wt% NaCl solution after 14 days of corrosion. An increase in the transfer resistance and a change of the double layer capacitance with increasing immersion duration were observed. The

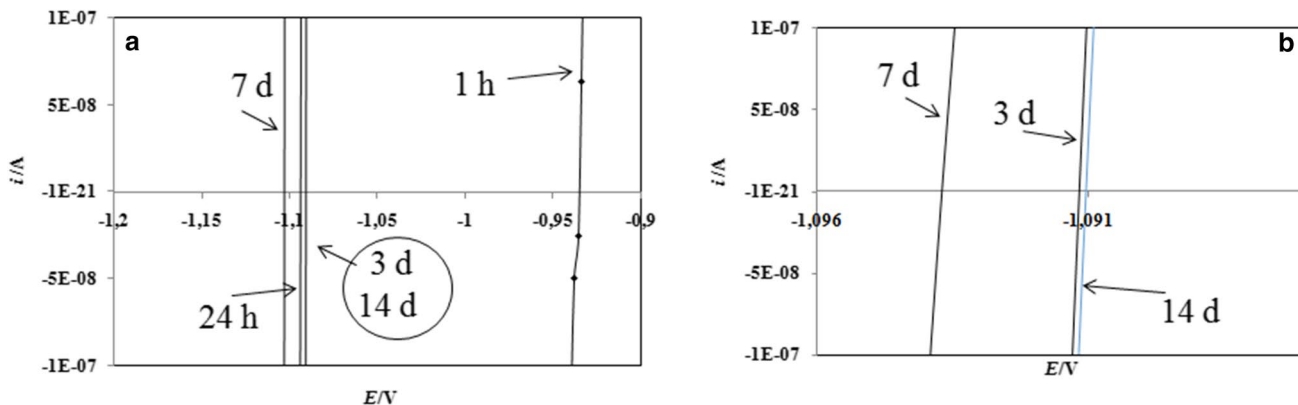


Fig. 17 Magnification of $i(E)$ curves of AlSi10Cu(Fe) sand cast aluminum alloy in 3 wt% NaCl solution after different immersion times

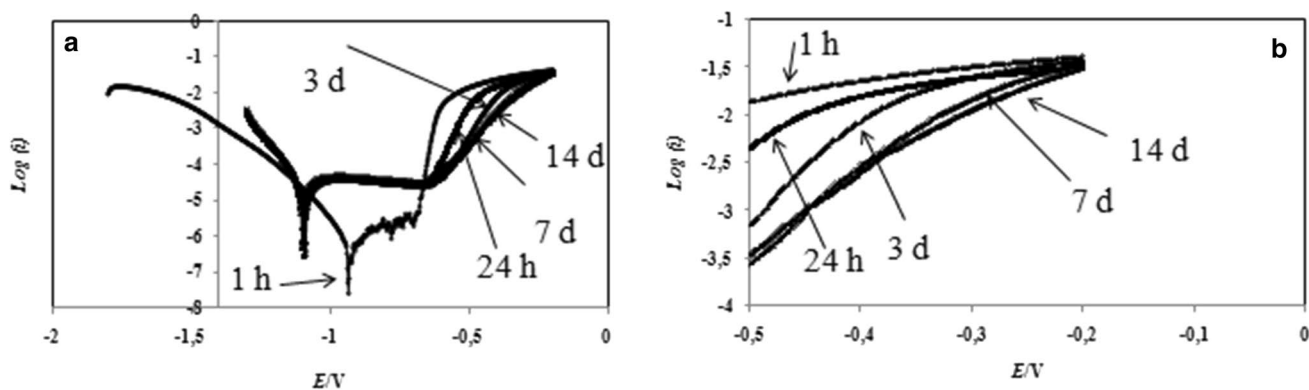


Fig. 18 Log $i(E)$ curves of AlSi10Cu(Fe) sand cast aluminum alloy in 3 wt% NaCl solution after different immersion times

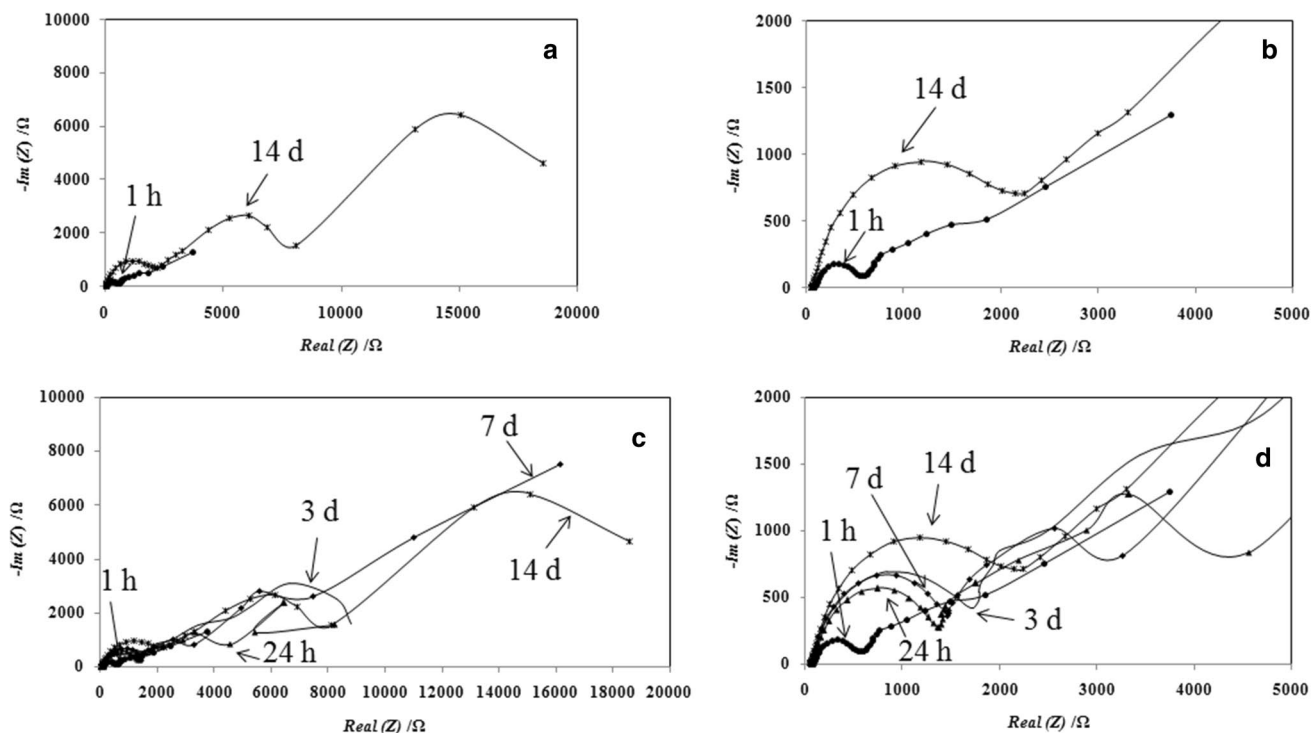


Fig. 19 **a** Nyquist plots of AlSi10Cu(Fe) sand cast aluminum alloy immersed in 0.3 wt% NaCl solution after 1 h of immersion and after 14 days of corrosion, **b** magnification of Nyquist plot of **a**, **c** after different immersion times, **d** magnification of Nyquist plot of **c**

change of double layer capacitance can be due to the presence of porosities on surface. The corrosion potential tends to -1.10 V after 14 days of corrosion in 0.3 and 3 wt% NaCl solutions. The polarization resistance is about 2.8 k Ω in the 0.3 wt% NaCl solution, and 1.4 k Ω in the 3 wt%

NaCl solution. Due to its high corrosion rate value, in the 3 wt% NaCl solution, the use of the alloy in sea water is not recommended. Wide passive windows, followed by the breakdown of passive film and excessive dissolution, were observed in 0.3% and 3 wt% NaCl solutions.

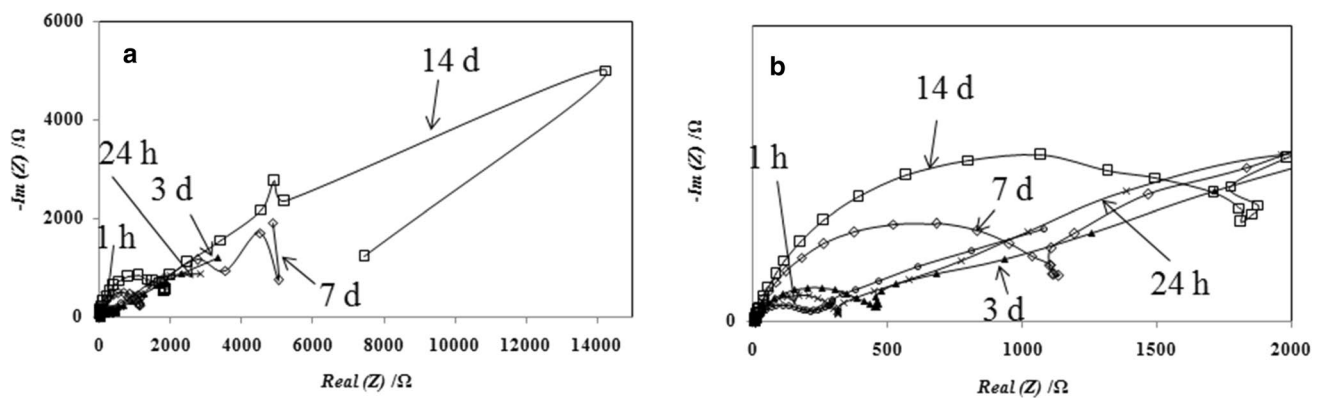


Fig. 20 a Nyquist plots of AlSi10Cu(Fe) sand cast aluminum alloy immersed in 3 wt% NaCl solution after different immersion times

Table 7 Corrosion potential, polarization resistance and corrosion current of the AlSi10Cu(Fe) sand cast aluminum alloy immersed in 0.3 wt% NaCl solution

Immersion time	E_{corr} (V/SCE)	R_p (k Ω)	i_{corr} ($\mu\text{A}/\text{cm}^2$)	V_{corr} (mm/year)
1 h	−0.583	2.5	3.8	0.044
24 h	−1.033	16.5	4.0	0.046
3 days	−1.11	2.7	14.1	0.162
7 days	−1.14	2.1	23.9	0.274
14 days	−1.10	2.8	15.0	0.172

Table 8 Corrosion potential, polarization resistance and corrosion rate of the AlSi10Cu(Fe) sand cast aluminum alloy immersed in 3 wt% NaCl solution

Immersion time	E_{corr} (V/SCE)	R_p (k Ω)	i_{corr} ($\mu\text{A}/\text{cm}^2$)	V_{corr} (mm/year)
1 h	−0.9350	21	1.5	0.017
24 h	−1.0933	2.1	33	0.375
3 days	−1.0917	0.5	34	0.385
7 days	−1.1046	1.1	41	0.466
14 days	−1.0921	1.4	34	0.385

Table 9 Solution resistance (R_s), transfer resistance (R_t) and double-layer capacitance (C_d) AlSi10Cu(Fe) sand cast aluminum alloy of immersion in 0.3 wt% NaCl versus time of immersion for sample area equal to 1 cm²

Immersion time	R_s (Ω)	R_t (Ω/cm^2)	C_d ($\mu\text{F}/\text{cm}^2$)
1 h	70	154	201
24 h	67	1616	136
3 days	59	2192	139
7 days	53	1898	230
14 days	53	2768	153

Table 10 Solution resistance (R_s), transfer resistance (R_t) and double layer capacitance (C_d) AlSi10Cu(Fe) sand cast aluminum alloy immersed in 3 wt% NaCl solution after different immersion times

Immersion time	R_s (Ω)	R_t (Ω/cm^2)	C_d ($\mu\text{F}/\text{cm}^2$)
1 h	11	271	587
24 h	12	260	613
3 days	9	542	407
7 days	7	1406	420
14 days	7	2536	323

References

- Ahn SS, Pathan S, Koo JM, Baeg CH, Jeong CU, Son HT, Kim YH, Lee KH, Hong SJ (2018) Enhancement of the mechanical properties in Al–Si–Cu–Fe–Mg alloys with various processing parameters. *Materials* 11:2150. <https://doi.org/10.3390/ma11112150>
- Al-Hella A, Kawther WA (2013) New approaches to casting hypereutectic Al–Si Alloys to achieve simultaneous refinement of primary silicon and modification of eutectic silicon, a thesis submitted for the degree of doctor of philosophy, Brunel center for advanced solidification technology (BCAST), Brunel university
- Allachi H, Chaouket F, Draoui K (2010) Protection against corrosion in marine environments of AA6060 aluminium alloy by cerium chlorides. *J Alloys Compd* 491:223–229. <https://doi.org/10.1016/j.jallcom.2009.11.042>
- Ambat R, Davenport AJ, Scamans GM, Afseth A (2006) Effect of iron-containing intermetallic particles on the corrosion behaviour of aluminium. *Corros Sci* 48:3455–3471. <https://doi.org/10.1016/j.corsci.2006.01.005>
- Ammar HR, Samiel AM, Samuel FA (2008) porosity and fatigue behavior of hypoeutectic and hypereutectic aluminum-silicon casting alloy. *Int J Fatigue* 30:1024–1035. <https://doi.org/10.1016/j.ijfatigue.2007.08.012>
- Bannour S, Abderrazak K, Mattei S, Masse JE, Autric M, Mhiri H (2013) The influence of position in overlap joints of Mg and Al alloys on microstructure and hardness of laser welds. *J Laser Appl* 25:032001. <https://doi.org/10.2351/1.4792615>
- Barr TL (1977) ESCA studies of naturally passivated metal foils. *J Vac Sci Technol* 14:660–665. <https://doi.org/10.1116/1.569174>

- Barrirero J, Pauly C, Engstler M, Ghanbaj J, Ghafoor N, Lin J, Schumacher P, Odén M, Mücklich F (2019) Eutectic modification by ternary compound cluster formation in Al–Si alloys. *Sci Rep*. <https://doi.org/10.1038/s41598-019-41919-2>
- Berlanga-Labari C, Biezma-Moraleda MV, Rivero PJ (2020) Corrosion of cast aluminum alloys: a review. *Metals* 10:1–29. <https://doi.org/10.3390/met10101384>
- Bessone JB, Salinas DR, Mayer Ebert CE, Lorenz WJ (1992) An EIS study of aluminium barrier-type oxide films formed in different media. *Electrochim Acta* 37:2283–2290. [https://doi.org/10.1016/0013-4686\(92\)85124-4](https://doi.org/10.1016/0013-4686(92)85124-4)
- Birbilis N, Buchheit RG (2005) Electrochemical characteristics of intermetallic phases in aluminum alloys. *J Electrochem Soc* 152:B140. <https://doi.org/10.1149/1.1869984>
- Bogdanoff T, Seifeddine S, Dahle AK (2016) The effect of Si content on microstructure and mechanical properties of Al–Si alloy. *La Metall Ital* 108:65–69
- Cáceres CH, Svensson IL, Taylor JA (2003) Strength-Ductility behaviour of Al–Si–Cu–Mg casting alloy in T6 temper. *Int J Cast Met Res* 15:531–543. <https://doi.org/10.1080/13640461.2003.11819539>
- Campbell J, Castings (2003) the new metallurgy of cast metals. 2nd edn, Oxford
- Cecchel S, Cornacchia G, Gelfi M (2017) Corrosion behavior of primary and secondary AlSi high pressure die casting alloys. *Mater Corros* 68:961–669. <https://doi.org/10.1002/maco.201709526>
- Ceschini L, Morri A, Morrin A, Toschi S, Johansson S, Seifeddine S (2015) Effect of microstructure and overaging on the tensile behavior at room and elevated temperature of C355-T6 cast aluminum alloy. *Mater Des* 83:626–634. <https://doi.org/10.1016/j.matdes.2015.06.031>
- Dinnis CM, Taylor JA, Dahle AK (2006) Interactions between iron, manganese, and the Al–Si eutectic in hypoeutectic Al–Si alloys. *Metall and Mater Trans A* 37:3283–3291. <https://doi.org/10.1007/BF02586163>
- Djurđević M, Stockwell T, Sokolowski J (1999) The effect of strontium on the microstructure of the aluminium–silicon and aluminium–copper eutectics in the 319 aluminium alloy. *Int J Cast Met Res* 12:67–73
- Dobkowska A, Adamczyk K, Cieślak D, Mizera B, Kurzydłowski KJ, Kiełbus A (2016) The comparison of the microstructure and corrosion resistance of sand cast aluminum alloys. *Arch Metall Mater* 61:209–212. <https://doi.org/10.1515/amm-2016-0038>
- Elzanaty H (2015) Effect of composition on the microstructure, tensile and hardness properties of Al–xSi alloys. *J Mater Sci Surf Eng* 2:126–129
- Fernandes JCS, Travassos MA, Leitão E, Rangel CM, Barbosa M, Ferreira MGS (1989) the influence of Li on the electrochemical behaviour of pure aluminium. *Portugaliae Electrochimica Acta* 7:119–122
- Ferreira IL, Lins JFC, Moutinho DJ, Gomes LG, Garcia A (2010) Numerical and experimental investigation of microporosity formation in a ternary Al–Cu–Si alloy. *J Alloys Compd* 503:31–39. <https://doi.org/10.1016/j.jallcom.2010.04.244>
- Frers SE, Stefanel MM, Mayer C, Chierchie T (1990) AC-Impedance measurements on aluminium in chloride containing solutions and below the pitting potential. *J Appl Electrochem* 20:996–999. <https://doi.org/10.1007/bf01019578>
- Hossain A, Gulshan F, Kurny ASW (2015) Electrochemical corrosion behavior of Ni-containing hypoeutectic Al–Si alloy. *J Electrochem Sci Eng* 5:173–179. <https://doi.org/10.5599/jese.174>
- Jafarzadeh K, Shahrabi F, Oskouei AA (2009) novel approach using EIS to study flow accelerated pitting corrosion of AA5083-H321 aluminium-magnesium alloy in NaCl. *J Appl Electrochem* 39:1725–1731. <https://doi.org/10.1007/s10800-009-9867-5>
- Jia Q, Li D, Li S, Zhang Z, Zhang N (2018) High-temperature oxidation resistance of NiAl intermetallic formed in situ by thermal spraying. *Coatings* 8:292. <https://doi.org/10.3390/coatings8080292>
- Jiang W, Fan Z, Dai T, Li C (2014) Effects of rare earth elements addition on microstructures, tensile properties and fractography of A357 alloy. *Mater Sci Eng A* 597:237–244. <https://doi.org/10.1016/j.msea.2014.01.009>
- Kuchariková L, Liptáková T, Tillová E, Bonek M, Medvecká D (2020) Corrosion behaviour correlation of the secondary aluminium casts in natural atmosphere and laboratory conditions. *Arch Metall Mater* 65:1455–1462. <https://doi.org/10.24425/amm.2020.133713>
- Li Z, Samuel AM, Samuel FH, Ravindran C, Valtierra S (2003) Effect of alloying elements on the segregation and dissolution of Al₂Cu phase in Al–Si–Cu 319 alloys. *J Mater Sci* 38:1203–1218. <https://doi.org/10.1023/A:1022857703995>
- Ma P, Jia Y, Prashanth K, Yu Z, Li C, Zhao J, Yang S, Huang L (2017) Effect of Si content on the microstructure and properties of Al–Si alloys fabricated using hot extrusion. *J Mater Res* 32:2210–2217. <https://doi.org/10.1557/jmr.2017.97>
- Mathers G (2002) The welding of aluminium and its alloys. CRC Press, Cambridge
- Mbuya TO, Odera BO, Ng'ang'a SP (2003) Influence of iron on castability and properties of aluminium silicon alloys: literature review. *Int J Cast Met Res* 16:451–465. <https://doi.org/10.1080/13640461.2003.11819622>
- McAlister AJ, Murray JL (1987) The (Al–Mn) aluminum-manganese system. *J Phase Equilib* 8:438–447
- Michna S, Lukac I, Louda P, Ocenasek V, Schneider H, Drapala J, Koreny R, Miskufova A (2007) Aluminum materials and technologies from A to Z, Adin, s.r.o. Presom, Czech Republic
- Mohamed AMA, Samuel FHA (2012) Review on the heat treatment of Al–Si–Cu/Mg casting alloys, heat treatment-conventional and novel applications. InTech: Rijeka, Croatia. <https://doi.org/10.5772/79832>
- Munoz AG, Bessone JB (1999) Pitting of aluminium in non-aqueous chloride media. *Corros Sci* 41:1447–1463. [https://doi.org/10.1016/S0010-938X\(98\)00199-1](https://doi.org/10.1016/S0010-938X(98)00199-1)
- Oya Y, Kojima Y, Hara N (2013) Influence of silicon on intergranular corrosion for aluminum alloys. *Mater Trans* 54:1200–1208. <https://doi.org/10.2320/matertrans.M2013048>
- Pourbaix M (1974) Atlas of electrochemical equilibria in aqueous solutions. National Association of Corrosion Engineers, Houston
- Reardon AC (2011) Metallurgy for the non-metallurgist, 2nd edn. ASM International, Materials Park
- Rossi S, Eyraud M, Vacandio F, Massiani Y (2007) Corrosivity of long-term fire retardant Fire Trol (R) 931 and Fire Foam (R) 103 on aluminium alloys and steel. *Mater Chem Phys* 105:260–267. <https://doi.org/10.1016/j.matchemphys.2007.04.055>
- Roy N, Samuel AM, Samuel FH (1996) Porosity formation in Al–9 wt pct Si–3 wt pct Cu alloy systems: metallographic observations. *Metall and Mater Trans A* 27:415–429. <https://doi.org/10.1007/bf02648419>
- Samuel EH, Samuel AM, Doty HW (1997) Factors controlling the type and morphology of Cu-containing phases in 319 Al alloy. *Trans Am Foundry Men's Soc* 30:893–801. <https://doi.org/10.1080/13640461.1999.11819344>
- Seri O, Furuya S, Soga N (1989) Effect of copper content on corrosion of aluminum. *J Jpn Inst Light Met* 39:724–729. <https://doi.org/10.2464/jilm.39.724>
- Singh S, Goel DB (1990) Influence of thermomechanical aging on tensile properties of 2014 aluminium alloy. *J Mater Sci* 25:3894–3900. <https://doi.org/10.1007/bf00582456>
- Sjölander E, Seifeddine S (2010) The heat treatment of Al–Si–Cu–Mg casting alloys. *J Mater Process Technol* 210:1249–1259. <https://doi.org/10.1016/j.jmatprotec.2010.03.020>

- Skoko Ž, Popović S, Štefanić G (2009) Microstructure of Al–Zn and Zn–Al Alloys. *Croat Chem Acta* 82:405–420
- Stadler F, Antrekowitsch H, Fragner W, Kaufmann H, Uggowitz PJ (2011) The effect of Ni on the high-temperature strength of Al–Si cast alloys. *Mater Sci Forum* 690:274–277. <https://doi.org/10.4028/www.scientific.net/MSF.690.274>
- Stadler F, Antrekowitsch H, Fragner W, Kaufmann H, Uggowitz PJ (2012) Effect of main alloying elements on strength of Al–Si foundry alloys at elevated temperatures. *Int J Cast Met Res* 25:215–224. <https://doi.org/10.1179/1743133612Y.0000000004>
- Taylor JA (1995) Metal-related castability effects in aluminium foundry alloys. *Cast Metals* 8:225–252. <https://doi.org/10.1080/09534962.1996.11819212>
- Taylor JA (2004) The effect of iron in Al–Si casting alloys. In: 35th Australian Foundry Institute National conference, Adelaide, South Australia 148
- Tenekedjiev N, Gruzleski JE (1990) Hypereutectic aluminium-silicon casting alloys—a review. *Cast Met* 3:96–105. <https://doi.org/10.1080/09534962.1990.11819026>
- Tillov E, Chalupov M, Hortalov L (2012) Evolution of phases in a recycled Al–Si cast alloy during solution treatment. *Scan Electron Microsc.* <https://doi.org/10.5772/34542>
- Warmuzek M (2004) Aluminum-silicon casting alloys: Atlas of microfractographs. ASM International Materials Park, Ohio
- Ye HZ (2003) An overview of the development of Al–Si-alloy based material for engine applications. *J Mater Eng Perform* 12:288–297. <https://doi.org/10.1361/105994903770343132>
- Yoo YH, Park IJ, Kim JG, Kwak DH, Ji WS (2011) Corrosion characteristics of aluminum alloy in bio-ethanol blended gasoline fuel: Part 1. The corrosion properties of aluminum alloy in high temperature fuels. *Fuel* 90:1208–1214. <https://doi.org/10.1016/j.fuel.2010.10.058>
- Zaid B, Saidi D, Benzaid A, Hadji S (2008) Effects of pH and chloride concentration on pitting corrosion of AA6061 aluminum alloy. *Corrosion Sci* 50:1841–1847. <https://doi.org/10.1016/j.corsci.2008.03.006>
- Zamani M, Seifeddine S, Jarfors AE (2015) High temperature tensile deformation behavior and failure mechanisms of an Al–Si–Cu–Mg cast alloy—the microstructural scale effect. *Mater Des* 86:361. <https://doi.org/10.1016/j.matdes.2015.07.084>
- Zazi N (2013) Effect of heat treatments on the microstructure, hardness and corrosion behavior of nondendritic AlSi₉Cu₃(Fe) cast alloy. *Mater Sci (Medžiagotyra)* 19:258–263. <https://doi.org/10.5755/j01.ms.19.3.1397>
- Zazi N, Bouabdallah A, Aaboubi O, Chopart JP (2010) Pretreatment effects on the electrochemical responses for aluminium–magnesium alloy AA5083 corrosion behavior. *Solid State Electrochem* 14:1705–1711. <https://doi.org/10.1007/s10008-010-1021-0>

Publisher's Note Springer Nature remains neutral with regard to jurisdictional claims in published maps and institutional affiliations.